JOURNAL OF GEOPHYSICAL RESEARCH: SOLID EARTH, VOL. 118, 4794–4813, doi:10.1002/jgrb.50349, 2013

Complex anisotropy beneath the Peruvian flat slab from frequency-dependent, multiple-phase shear wave splitting analysis

Caroline M. Eakin[1] and Maureen D. Long[1]

Received 5 October 2012; revised 16 August 2013; accepted 19 August 2013; published 10 September 2013.

[1] Flat or shallow subduction is a relatively widespread global occurrence, but the dynamics remain poorly understood. In particular, the interaction between flat slabs and the surrounding mantle flow has yet to be studied in detail. Here we present measurements of seismic anisotropy to investigate mantle flow beneath the Peruvian flat-slab segment, the largest present-day region of flat subduction. We conduct a detailed shear wave splitting analysis at a long-running seismic station (NNA) located near Lima, Peru. We present measurements of apparent splitting parameters (fast direction ϕ and delay time δt) for *SKS*, *ScS*, and local *S* phases from 80 events. We observe well-defined frequency dependence and backazimuthal variability, indicating the likely presence of complex anisotropy. Forward modeling the observations with two or three layers of anisotropy reveals a likely layer with a trench-normal fast direction underlying a layer with a more trench-oblique (to trench-subparallel) fast direction. In order to further constrain the anisotropic geometry, we analyzed the source-side splitting from events originating within the slab measured at distant stations. Beneath the flat-slab segment, we found trench-normal fast splitting directions in the subslab mantle, while within the dipping portion of the slab further to the east, likely trench-subparallel anisotropy within the slab itself. This subslab pattern contradicts observations from elsewhere in South America for "normal" (i.e., more steeply dipping) slab conditions. It is similar, however, to inferences from other shallowly dipping subduction zones around the world. While there is an apparent link between slab dip and the surrounding mantle flow, at least beneath Peru, the precise nature of the relationship remains to be clarified.

Citation: Eakin, C. M., and M. D. Long (2013), Complex anisotropy beneath the Peruvian flat slab from frequency-dependent, multiple-phase shear wave splitting analysis, *J. Geophys. Res. Solid Earth*, *118*, 4794–4813, doi:10.1002/jgrb.50349.

1. Introduction

[2] "Flat" or "shallow" slabs represent around 10% of subduction zones worldwide today [*Gutscher et al.*, 2000]. Extending over 1500 km along strike, the Peruvian flat-slab segment (3°S to 15°S) is by far the most extensive present-day region of flat subduction (Figure 1). The slab subducts normally to a depth of around 100 km, most likely directly beneath the overriding continental lithosphere [*Cahill and Isacks*, 1992], and travels horizontally for several hundred kilometers before steepening again to the east. The region is characterized by a distinct lack of contemporary volcanism and low heat flow (~20 mW/m^2) [*Henry and Pollack*, 1988], in contrast to the normally dipping (~30°) regions to the north and south. Subduction has been operating along the western coast of Peru since at least the Jurassic [*Martinod et al.*, 2010], but the slab is thought to have flattened only during the Miocene (~12 Ma), when arc volcanism died out in an easterly progression [*Aleman*, 2006; *Ramos and Folguera*, 2009]. The timing of Peruvian slab flattening is fairly well known, but the cause is far less clear.

[3] Flat slabs have commonly been associated with the subduction of anomalous features on the subducting seafloor, such as oceanic plateaus that exhibit over-thickened crust and thus increased buoyancy [e.g., *Gutscher et al.*, 2000]. For Peru in particular, the emergence of flat-slab subduction is believed to have coincided with the arrival of the Nazca ridge, an aseismic ridge feature on the Nazca plate (Figure 1), on the Peruvian coast around 11–15 Ma at a latitude between 9°S and 11°S [*Hampel*, 2002; *Rosenbaum et al.*, 2005]. Due to the oblique orientation between the ridge and the trench, the Nazca ridge has since been moving south through the subduction zone to its current position between 14°S and 17°S [*Hampel*, 2002]. For the northern end of the flat-slab region, which was never affected by Nazca ridge subduction, it has been suggested that an elusive feature known as the Inca Plateau was subducted there. Any direct evidence for this feature has long since disappeared, but it may represent a conjugate of the Marquesas plateau on the Pacific plate [*Gutscher et al.*, 1999a, 1999b].

[4] There are, however, several potential problems with this model for flat-slab formation, both for Peru and for other subduction systems. First, the thickened oceanic crust is

Additional supporting information may be found in the online version of this article.

[1]Department of Geology and Geophysics, Yale University, New Haven, Connecticut, USA.

Corresponding author: C. M. Eakin, Department of Geology and Geophysics, Yale University, PO Box 208109, New Haven, CT 06520, USA. (caroline.eakin@yale.edu)

2169-9313/13/10.1002/jgrb.50349

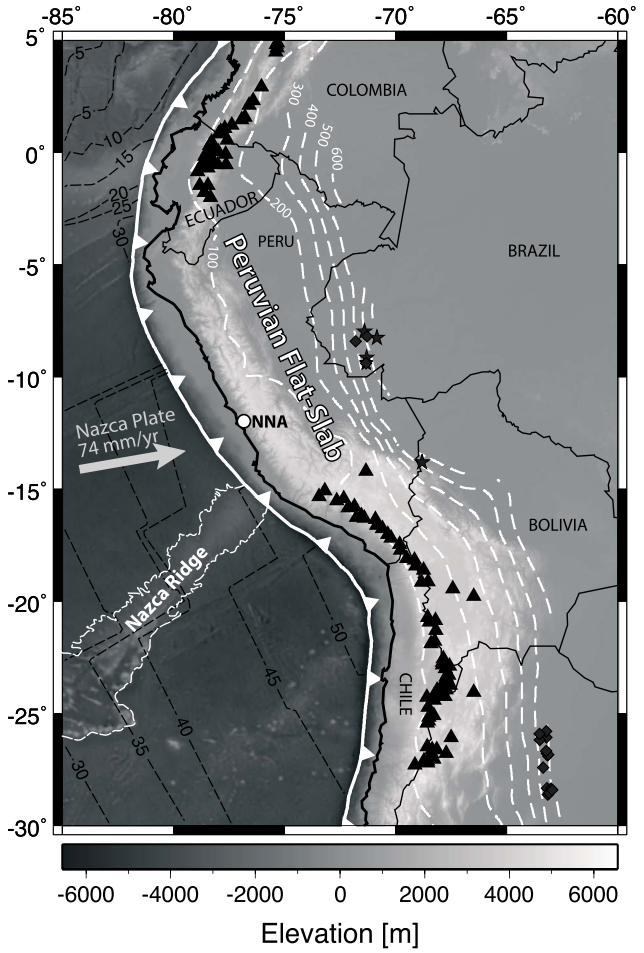

Figure 1. Tectonic map of the Peruvian flat-slab region. Thick white dashed lines are slab contours (unit: km) from the model Slab1.0 [*Hayes et al*., 2012]. Thin black dashed lines are contours of seafloor age (unit: Ma) [*Müller et al*., 2008]. Gray arrow represents the absolute plate motion of the Nazca plate from HS3-NUVEL1A [*Gripp and Gordon*, 2002]. Locations of volcanoes are represented by triangles [*Siebert and Simkin*, 2002]. Seismic station NNA located in the flat-slab region is plotted as a white dot. Source locations of local *S* and *ScS* events used in this study shown by small dark gray stars and diamonds.

mainly composed of basalt, which under equilibrium conditions will transform to higher-density eclogite at ~70–80 km depth [*Kirby et al*., 1996]. Considering that flat slabs generally lie at a depth of ~100 km, an over-thickened oceanic crust will not help generate a flat slab unless the transition to eclogite is significantly delayed [*van Hunen et al*., 2002]. An adequate potential mechanism for the slowing of the eclogization reaction has yet to be proposed. Second, the spatial correlation between flat slabs and impacting anomalous seafloor features is imperfect. Recent detailed work by *Skinner and Clayton* [2011, 2013] has shown that the global correlation between impactors and regions of flat subduction is frequently poor; furthermore, the reconstructed Inca Plateau does not match up well with northern Peru.

[5] Therefore, while the subduction of buoyant oceanic features may contribute to the development of some flat slabs, additional dynamic factors may be needed to sustain flat subduction, and specific questions regarding the origin and evolution of the Peruvian flat-slab segment remain to be answered. One aspect of flat-slab subduction that has yet to be studied in detail is how the surrounding mantle flow interacts with the flat-subduction system. Could mantle flow have a role in providing dynamic support to flat slabs? Are mantle dynamics and the pattern of mantle flow different in a flat-slab system in comparison to "normal" subduction conditions? In order to begin to answer such questions, we first need to identify the pattern of mantle flow beneath the Peruvian flat slab via an investigation of the seismic anisotropy in the flat-slab region. This task is not straightforward, however, given the presence of multiple possible sources of anisotropy (overriding plate, mantle wedge, slab, and subslab mantle) that may exist within a subduction zone. Understanding the subduction system as a whole thus requires careful consideration of the anisotropic contribution from each individual component. In this paper we present measurements of *SKS*, *ScS*, and local *S* phases at permanent station NNA, which is located in the central part of the Peruvian flat-slab system. We also investigate the splitting of teleseismic *S* phases originating from slab earthquakes, which are mainly sensitive to anisotropy in the subslab mantle. Our goal is to place constraints on seismic anisotropy within, beneath, and above the Peruvian flat slab to interpret the anisotropy in terms of mantle flow patterns and ultimately to understand what role, if any, ambient mantle flow plays in flat-slab subduction beneath Peru.

2. Shear Wave Splitting: Methods and Data

2.1. Seismic Anisotropy: Background

[6] Seismic anisotropy, or the directional dependence of seismic wave speed, is a key seismological observable, and the upper mantle represents one of the most important anisotropic regions in the Earth. In the upper mantle, anisotropy results mainly from the lattice preferred orientation (LPO) of olivine [e.g., *Montagner and Tanimoto*, 1990, 1991; *Gaherty and Jordan*, 1995; *Zhang and Karato*, 1995]. LPO describes a nonrandom distribution of crystallographic axes and results from deformation in the dislocation creep regime [e.g., *Karato*, 2008]. If the relationship between deformation and the resulting olivine LPO fabric is known, then interpretations of the mantle flow field can be made based on observations of seismic anisotropy.

[7] There are several known possible olivine LPO types, namely A-, B-, C-, D- and E-type fabric [e.g., *Katayama et al*., 2004; *Karato et al*., 2008]. AG-type fabric has also been documented, although its occurrence is rare in natural mantle-derived rocks [*Mainprice*, 2007]. For a given strain field, each LPO type represents different 3-D orientations of the olivine crystallographic axes that occur under different physical and chemical conditions. The exact relationship between the strain geometry and the resulting anisotropy will thus vary throughout the Earth's interior. Under conditions typical of the upper mantle, the A-, C-, or E-type fabrics are most likely to be present, and for all three fabrics the fast *a* axes of olivine tend to align parallel to the maximum strain direction [*Karato et al*., 2008]. For the simple case of horizontal mantle flow with a vertical gradient in flow velocity, the fast direction of anisotropy will therefore correspond to the mantle flow direction. For B-type fabric, which may be

Table 1. List of Parameters Relevant to the Search for Suitable Events for Shear Wave Splitting Analysis

Phase	Distance Range (deg)	Magnitudes (M_w)	Depths (km)	Number of Events Which Fit Criteria	Initial Polarization Range (deg)
SKS	88–130	> 6.0	any	588	235–255 [a]
Local *S*	0–10 [b]	> 4.5	> 70	10	230–260 [a]
ScS	0–35	> 5.0	> 500	44	40–75 and 200–245

[a]Applies to the vast majority of events.
[b]Inclination must also be < 35° to prevent phase conversion at the surface [e.g., *Savage*, 1999].

expected in the high-stress, low-temperature, water-rich forearc corner of the mantle wedge [*Kneller et al*., 2005], the fast axis of olivine aligns in the shear plane but perpendicular to the shear direction. For this olivine fabric geometry, the fast direction of anisotropy is oriented 90° from the mantle flow geometry [*Jung and Karato*, 2001]. Given that the Peruvian flat slab likely lies directly beneath the overlying continental lithosphere, based on the distribution of seismicity [*Cahill and Isacks*, 1992] and the lack of contemporary arc volcanism, there is thought to be little or no mantle wedge material in the area. The presence of significant volumes of B-type olivine fabric is therefore considered unlikely (although it cannot be entirely ruled out), and we assume that for the most part the relationships between deformation and anisotropy are typical of A-type (or similar) olivine fabric.

2.2. Shear Wave Splitting Measurement Method

[8] The measurement of shear wave splitting represents a popular and well-established technique for characterizing seismic anisotropy in the upper mantle. When a shear wave travels through an anisotropic medium, it is polarized into fast and slow components that are effectively orthogonal to one another and are recorded as separate quasi-*S* arrivals on a seismogram. Due to the difference in wave speed, the fast and slow arrivals accumulate a delay time between them that reflects the strength of anisotropy and/or the length of the raypath through the anisotropic material. During shear wave splitting analysis we aim to measure this delay time (δt) as well as the orientation of the fast direction (ϕ), which contains information about the geometry of anisotropy.

[9] We carried out shear wave splitting measurements using the SplitLab software package [*Wüstefeld et al*., 2008], which implements three different measurement methods to estimate a fast direction and delay time for each arrival. These are the transverse component energy minimization method (which we abbreviate SC after *Silver and Chan* [1991]), the rotation-correlation method (abbreviated RC) [e.g., *Bowman and Ando*, 1987], and the eigenvalue method (EV) [*Silver and Chan*, 1991]. Using multiple independent methods for estimating the fast direction and delay time is useful for determining the reliability of the result [e.g., *Levin et al*., 2004; *Wirth and Long*, 2010]. In this paper we report *SKS* splitting parameter estimates obtained using the SC method, as it is the most stable over a range of backazimuths [*Wüstefeld and Bokelmann*, 2007]. For direct *S* phases (local *S* and *ScS*) that have not passed through the outer core, the SC method is less straightforward to apply, as the initial polarization direction does not correspond to the backazimuth. In such cases the initial polarization can be predicted from the focal mechanism, and the SC (energy minimization) method can be applied to the component orthogonal to the initial polarization direction [e.g., *Marson-Pidgeon and Savage*, 2004]. In our analysis of direct *S* phases, however, we applied only the EV and RC methods and checked them for consistency; splitting parameters reported are obtained using the RC method.

[10] Every shear wave splitting measurement reported was also assessed for its quality. Only those measurements classified as "good" or "fair" are presented. During classification, following the procedure of *Eakin et al*. [2010], many different factors were taken into account. These include qualitative measures such as whether the shear phase (e.g., *SKS*) displays a similar shape in the estimated fast and slow directions, whether the corrected shear phase shows very little energy on the transverse component, and whether the originally elliptically polarized shear waves have a linear polarization after correction. Classification was also dependent on quantitative measures. The signal-to-noise ratio of the uncorrected transverse component was required to be greater than 5, and errors of less than 1 s for δt and 22.5° for ϕ at the 95% confidence level were necessary. Finally, we assessed the agreement in splitting parameter estimates between SC and RC methods for *SKS* phases or RC and EV methods for direct *S* phases. We evaluated whether the difference in fast direction ($|\Delta\phi|$) was less than 22.5° and the ratio of delay times ($\delta t_{RC}/\delta t_{SC}$) was greater than 0.7 [*Wüstefeld and Bokelmann*, 2007]. In order for a measurement to be retained and classified as at least fair, we required that the split shear wave pulse was clearly identifiable and all of the above conditions were met for the SC method analysis for *SKS* or the RC method for direct *S* phases. A good classification was given when stricter limits on the error bounds were met; specifically, we required small elliptical error spaces of less than 0.5 s for δt and ~10° for ϕ in addition to very similar estimates of the splitting parameters between methods ($|\Delta\varphi|$ ~10° and $|\delta t| < 0.3$ s).

[11] In the case of nulls, these were identified when a clearly visible shear phase with high signal-to-noise ratio (SNR > 5) produced uncorrected initial particle motion that was already linearized. Such a result suggests that the shear wave has not undergone any splitting. This may result from a lack of anisotropy (i.e., the underlying medium is isotropic), strong anisotropic heterogeneity, or alignment between the incoming initial polarization of the wave and the fast or slow axis of anisotropy.

2.3. Data: Station and Event Availability

[12] The only broadband station located over the Peruvian flat slab that is currently openly available for download from the Incorporated Research Institutions for Seismology Data Management System (www.iris.edu) is the long-running permanent station NNA (Figure 1), which belongs to the Global Seismographic Network (network code II). Our receiver-side analysis is therefore limited to a single station for the time being; however, data from NNA is of excellent quality, and there are over two decades' worth of data available. This seismic station began recording in 1988, and its remarkably long operating time allowed us to investigate the shear wave splitting signature in the upper mantle beneath NNA in great

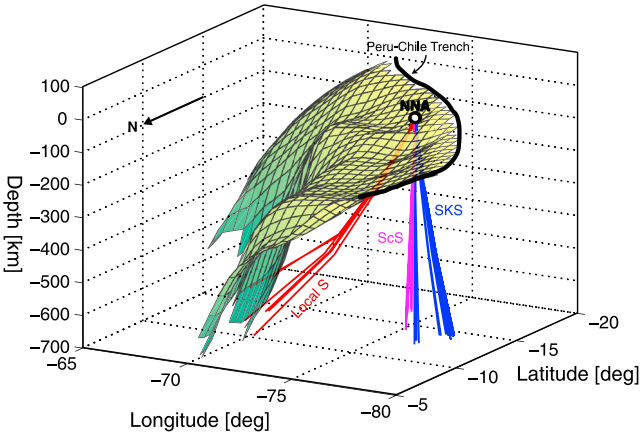

Figure 2. Raypath geometry of *SKS* (blue), *ScS* (magenta), and local *S* (red) shear waves that were recorded at NNA (white dot). Incidence of incoming phases were determined using TauP [*Crotwell et al*., 1999]. Model of the subducting slab surface from *Hayes et al*. [2012].

detail. We looked at data for three different shear wave phases measured at NNA: *SKS*, local direct *S*, and, *ScS*. The search parameters used when identifying events for each type of phase are listed in Table 1. A large number of earthquakes (588) were available in the distance range suitable for *SKS* analysis, but they are mostly located in a narrow backazimuth range in the southwest quadrant, corresponding to earthquakes in Tonga. The data set, however, is complimented by the *ScS* phases which have events covering a wider azimuth range.

[13] In order to compare results from the three phase types, we must consider their respective paths from the source to the receiver, shown in the diagram in Figure 2. *SKS* waves travel through the outer core as a *P* wave, are converted to an *S* wave at the core-mantle boundary (CMB), and arrive at the station with close to vertical incidence (usually less than 10° from the vertical). Similarly, *ScS* phases from the epicentral distance range used in this study (0°–35°) also arrive with near vertical incidence (up to 10° from vertical), but their paths are different; the events originate within the Andean subducting slab and then bounce off the CMB. We restrict our *ScS* analysis to very deep events (>500 km) to minimize the possibility of contamination from anisotropy near the source, but it is important to keep in mind that *ScS* phases may still contain a signal from anisotropy outside the study region. Local *S* phases, on the other hand, arrive at shallower incidence angles (up to 35° from vertical) and follow a different path through the upper mantle (Figure 2). Due to the geometry of the Peruvian flat slab and the source locations of the events yielding direct local *S* phases for analysis, most of the direct *S* arrivals sample the same subduction zone components as *SKS* and *ScS* (subslab mantle, slab, overriding continental plate), albeit along a different path (Figure 2).

[14] For *SKS*, the initial polarization of the shear wave (before it is affected by anisotropy) is known as it is equal to the backazimuth, but for *ScS* and local *S* it must be measured directly from the seismogram. If the splitting delay time is sufficiently smaller than the dominant period of the phase, then the initial polarization direction is preserved along the long axis of the ellipse in the uncorrected particle motion [*Long and Silver*, 2009b; *Vidale*, 1986]. In order to be confident that this condition has been satisfied, we report initial polarization estimates based on band-pass filtered seismograms using low corner frequencies (0.01–0.1 Hz). We also tested the robustness of this estimate using our *SKS* data set by comparing estimates of initial polarization to the known backazimuths (Figure 3, top). For all *SKS* events the difference was less than 10°. We note that this procedure is different from the "estimate polarization" option available in SplitLab, which uses the corrected seismograms to determine the polarization. With the estimate polarization option, any frequency dependence in the measured splitting parameters will affect the rotation and time shift applied to "correct" the waveforms. Estimating initial polarizations this way may therefore produce different values with different band-pass filters. Using the uncorrected particle motion instead, measured at low frequencies, results in a more robust estimate of initial polarization direction. As a secondary check, we also predicted the initial polarizations for *ScS* and local *S* events from their focal mechanisms [e.g., *Marson-Pidgeon and Savage*, 2004]. A comparison of the two methods of estimating initial polarization is shown in Figure 3 (bottom). For the majority of the arrivals (39 out of 47) the difference is less than 25°. However, we identified eight arrivals for which the disagreement was larger, and we removed these corresponding events from our data set.

3. Splitting Measurement Results for *SKS*, *ScS*, and Local *S*

[15] We initially performed shear wave splitting analyses for *SKS* phases, and our analysis yielded 71 results of acceptable

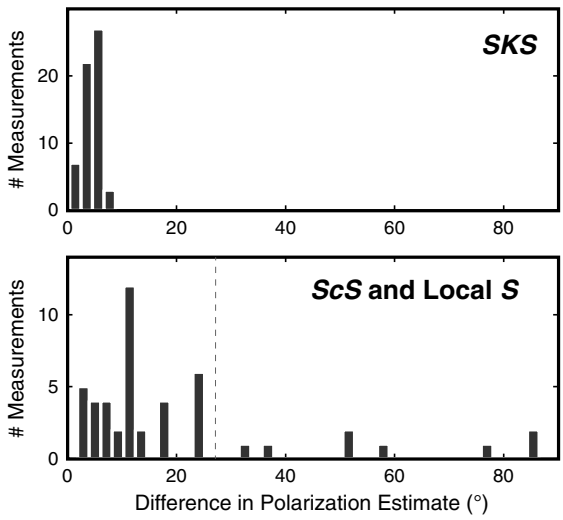

Figure 3. Comparison between different methods for estimating the initial polarization of shear arrivals. (top) The angular difference between the initial polarization of *SKS* phases estimated from the uncorrected particle motion and the known backazimuth of *SKS* events; this is always less than 10° for our data set. (bottom) The difference between initial polarizations estimated from the uncorrected particle motion and those predicted from the event focal mechanisms. Events for which this difference is greater than 25° (to the right of the dashed line) have been excluded from the splitting data set.

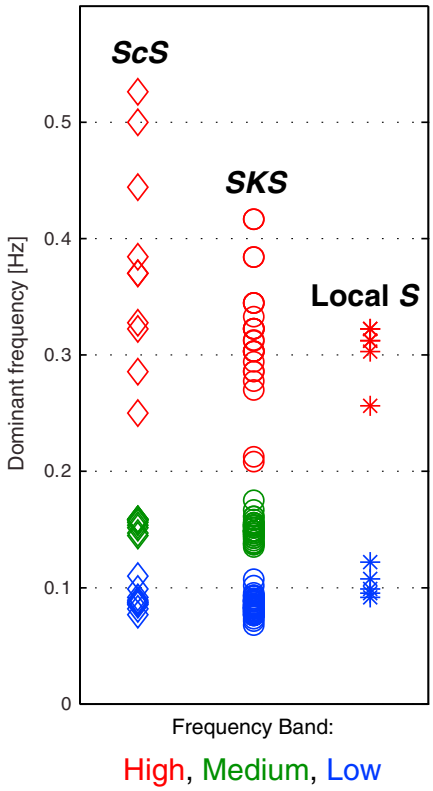

Figure 4. Estimates of dominant frequency of each phase for which a splitting measurement has been made, as inferred from the period of the selected shear wave pulse on the seismogram. Blue symbols represent low-frequency measurements, filtered between 0.01 and 0.1 Hz; green symbols are the medium frequencies filtered between 0.1 and 0.2 Hz; and the red symbols are the high frequencies filtered between 0.2 and 1.0 Hz (except for local *S* which were filtered between 0.1 and 0.4 Hz). In each frequency group (i.e., for each color) across all the three phases, the average frequency content is generally similar, although the high-frequency band does display some variability.

quality (i.e., classified as either good or fair), with average $\phi = -55.8°$, average $\delta t = 1.5$ s, and standard deviations: $\phi = 36.4°$, $\delta t = 0.3$ s (SW quadrant had 60 measurements: mean $\phi = -50.5°$, mean $\delta t = 1.5$ s, and standard deviations: $\phi = 8.5°$, $\delta t = 0.3$ s. NW quadrant had 11 measurements: mean $\phi = -85.0°$, mean $\delta t = 1.5$ s, and standard deviations: $\phi = 16.7°$, $\delta t = 0.4$ s). Only a small handful of nulls were identified (six nulls compared to 71 non-null measurements). Given their small proportion in our data set and the nuances in their interpretation (nulls can indicate a lack of anisotropy, strong anisotropic heterogeneity, or an initial polarization that is parallel to either the fast or slow direction), we chose to focus our further analysis only on the non-null measurements. Initially, we applied a band-pass filter during preprocessing with corner frequencies that ranged from 0.1 Hz or above on the high end and 0.04 Hz or below on the low end that were manually adjusted for each seismogram to increase the signal-to-noise ratio. The average *SKS* splitting parameters found here agree well with previously published results for NNA, which were based on only a few years' worth of data [*Helffrich et al.*, 1994; *Kaneshima and Silver*, 1995; *Russo and Silver*, 1994]. Our data set thus represents a considerable improvement over previous work; for example, *Helffrich et al.* [1994] measured splitting for five *SKS* arrivals, compared to 71 in our initial *SKS* data set. In these previous studies and in our own work the majority of events arrive from the SW quadrant and yield remarkably consistent splitting parameters (average $\phi = -50.5°$, average $\delta t = 1.5$ s). We did, however, also obtain a small number of *SKS* measurements from the NW quadrant (11 out of 71 total), and these produce more E-W oriented fast splitting directions (average $\phi = -85.0°$, average $\delta t = 1.5$ s), indicating that backazimuthal variability is present.

[16] During the application of our variable filter in the initial stage of *SKS* splitting analysis, we noticed a systematic change in the estimated splitting parameters with frequency content. In order to better characterize this observation, we repeated the *SKS* splitting measurements in three different frequency bands: 0.01–0.1 Hz (low), 0.1–0.2 Hz (medium), and 0.2–1.0 Hz (high). These filters were chosen based on the frequency content of the incoming *SKS* arrivals and are similar to those used by an earlier study of *SKS* frequency dependence in the Gulf of California [*Long*, 2010]. To characterize the dominant frequency of the phase arrivals within each band-pass group, we measured the half period between the peak and trough of each arrival and converted to frequency. The overall frequency content of our splitting data set is shown in Figure 4. In general, the dominant frequencies within each subset of filtered results are very similar. The averages are 0.09 Hz for the low band pass, 0.15 Hz for the medium band pass, and 0.33 Hz for the high band pass.

[17] Examples of diagnostic plots illustrating the typical nature of the frequency dependence in the shear wave splitting measurements are shown in Figure 5. The results of the full analysis, shown in Figure 6 (open circles correspond to *SKS* measurements), yielded unequivocal evidence for both frequency dependence and backazimuthal variability of apparent *SKS* splitting parameters. Focusing in particular on the *SKS* results from the SW quadrant plotted in Figure 6c, we found that not only is each frequency band associated with an offset in average fast direction, but we also observed a systematic rotation of the fast direction with increasing backazimuth at each frequency. Such a precise, systematic variation in measured splitting parameters with frequency has not previously been documented using *SKS* phases to our knowledge, and only a few studies have found evidence for frequency-dependent *SKS* splitting [e.g., *Marson-Pidgeon and Savage*, 1997, 2004; *Long*, 2010]. Plots of delay time with respect to backazimuth, shown in Figure 6d, also show clear frequency dependence, which manifests especially clearly in the difference between the low-frequency band (δt ~1.5–2.25 s) and the medium/high-frequency bands (δt ~ 0.75–1.5 s).

[18] In order to improve the limited coverage in initial polarization direction of our *SKS* data set, we made additional splitting measurements using local *S* and *ScS* phases. These are also plotted as a function of frequency and backazimuth in Figure 6. We used the same set of band-pass filters in the preprocessing as for the *SKS* analysis, except for local *S*: for this phase we found very small signal amplitudes in either the medium (0.1–0.2 Hz) or high (0.2–1.0 Hz) frequency bands, so they were combined into a single band pass covering 0.1–0.4 Hz. Figure 4 shows that these local *S* measurements (red asterisks) have a dominant frequency of around

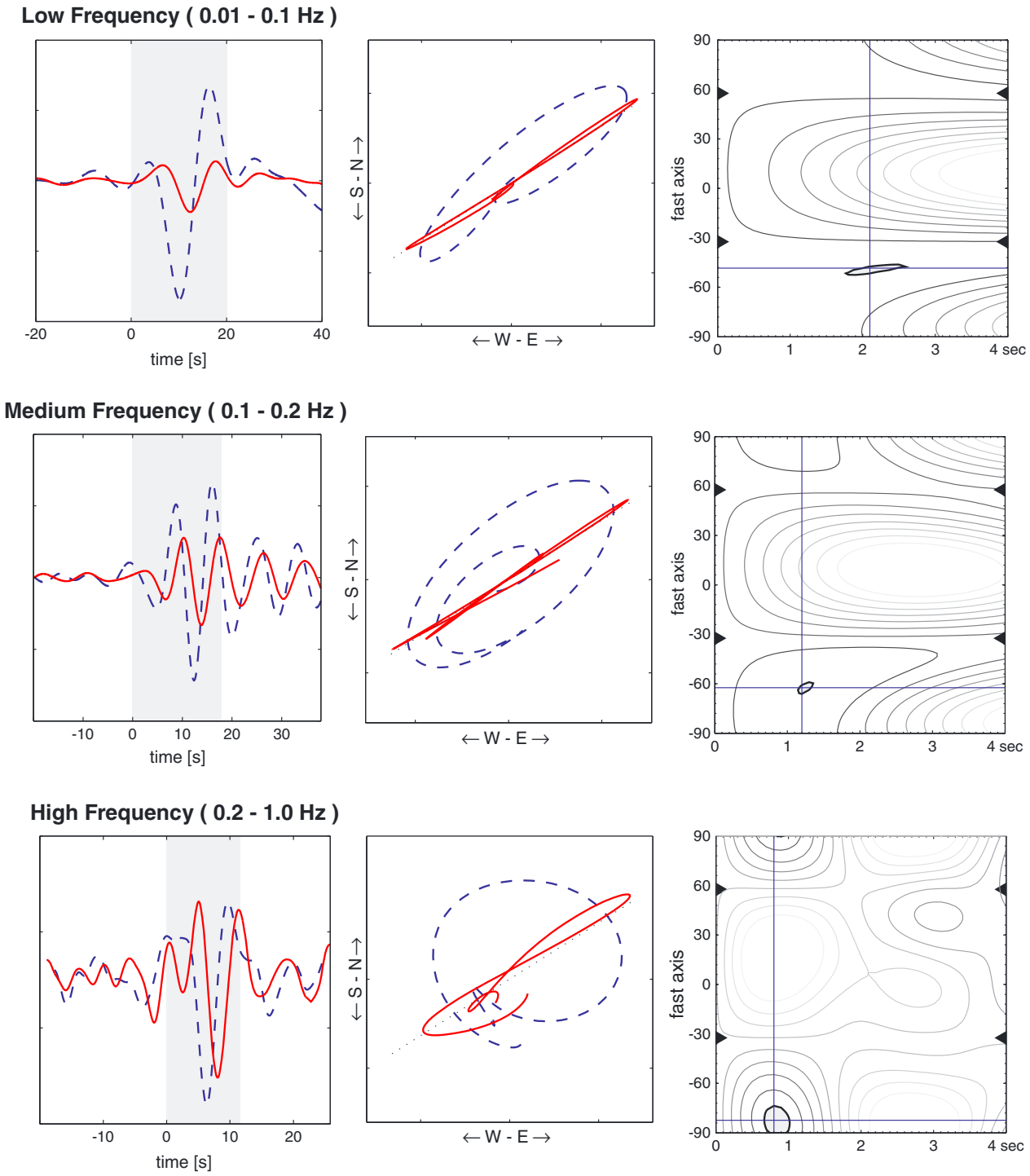

Figure 5. Example of frequency-dependent shear wave splitting measurements at NNA from a M_w 6.9 event located in Tonga (14:45 09 July 1998). All three rows show the same *SKS* waveform filtered at different frequencies. (for each row, from left to right) The uncorrected radial (dashed) and transverse (solid) components are shown (left box) with the selected time window shaded gray, alongside (middle box) the uncorrected (dashed) and corrected (solid) particle motion, and (right box) the error space predicting fast direction (degrees from north) and delay time via the SC method [*Silver and Chan*, 1991]. The sizes of the error spaces (gray circle representing the 95% confidence region) are small and tightly constrained. In the low-frequency band (top row) the splitting parameters are ϕ: $-54 < -48° < -48$, δt: $1.8 < 2.1$ s 2.6. In the medium-frequency band (middle row) the splitting parameters are ϕ: $-68 < -62° < -62$, δt: $1.1 < 1.2$ s < 1.4. In the high-frequency band (bottom row) the splitting parameters are ϕ: $-92 < -82° <$ 76, δt: $0.7 < 0.8$ s < 1.0. Therefore, in this example as the period decreases (from top to bottom) the fast direction rotates from NW-SE to more E-W, and the delay time drops from > 2 to < 1 s.

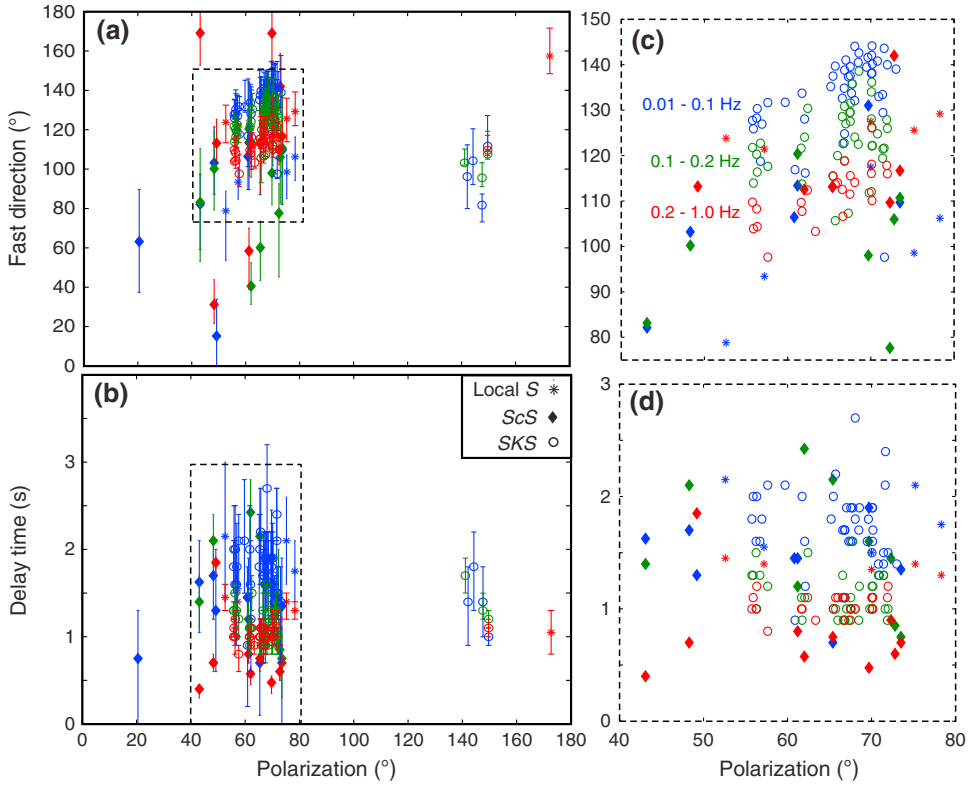

Figure 6. Results of shear wave splitting at NNA. Open circles: *SKS*, colored diamonds: *ScS*, asterisks: local *S*. Blue: low-frequency band (0.01–0.1 Hz), green: medium-frequency band (0.1–0.2 Hz), red: high-frequency band (0.2–1.0 Hz). For local *S* the red asterisks represent a slightly different frequency band 0.1–0.4 Hz. (a) Fast direction as a function of initial polarization, (b) delay time as a function of initial polarization, (c) zoomed in region of Figure 6a represented by dashed box, (d) zoomed in region represented by dashed box in Figure 6b.

0.3 Hz and are therefore most comparable to other results from the high band-pass group (0.2–1.0 Hz) plotted as red symbols. Most of the initial polarizations of the local *S* and *ScS* happen to lie in the azimuth interval (40°–90°). This is where the *SKS* measurements are also located, after mapping to 0°–180° range, making them easy to compare.

[19] In terms of fast direction (Figures 6a and 6c), there is clear disagreement between the local *S* and *SKS* results in both the low and high-frequency bands. In the high-frequency band the local *S* results (red asterisks) are more similar to the *SKS* from the medium-frequency band (green circles), but in the low-frequency band there is little agreement between the local *S* results and any of the *SKS* results. The frequency dependence pattern in ϕ is therefore inverted for local *S*: that is, the fast direction angle decreases as the frequency decreases, whereas the opposite is true for *SKS*. The *ScS* results cover a broader azimuth range and are more variable, with systematic trends less easy to identify. In some cases there is partial agreement, for example, between most of the high-frequency *ScS* (red diamonds) and high-frequency *SKS* (red circles) results in Figure 6c. However, there are also some discrepancies, for example, the abundance of medium- and low-frequency *ScS* (green and blue diamonds) surrounding the high-frequency *SKS* (red circles) results in Figure 6c. The *ScS* results are more scattered than the other phases, possibly due to errors inherent in estimating the initial polarization and/or to possible source-side contamination.

[20] In terms of delay time (Figures 6b and 6d), there is much more agreement between the different phases than for the fast directions. For all the phases, the highest frequency measurements display smaller delay times than lowest frequency measurements. In Figure 6d, there is only one measurement from the high-frequency band (red *ScS* diamond) with a delay time above 1.5 s; likewise, there are only three measurements from the low-frequency band (two blue *SKS* circles and one blue *ScS* diamond) with delay times below 1.25 s. Even within the high-frequency group (red symbols), *ScS* results tend to have smaller delay times than *SKS*, which in turn tend to have smaller delay times than local *S* results. This appears to reflect the frequency content of each phase; Figure 4 shows that within the high band-pass group the average frequency of *ScS* measurements is higher than *SKS*, which in turn is higher than local *S*. In both the medium- and low-frequency bands, however, there is very little difference between the average frequency content of each phase (Figure 4) which appears to also result in similar delay times (Figure 6d). Overall, our results show strong frequency dependence in delay time, with lower frequency measurements on average producing larger delay times.

4. Modeling Multiple Layers of Anisotropy

[21] Previous shear wave splitting studies over the Peruvian flat-slab region have identified a handful of

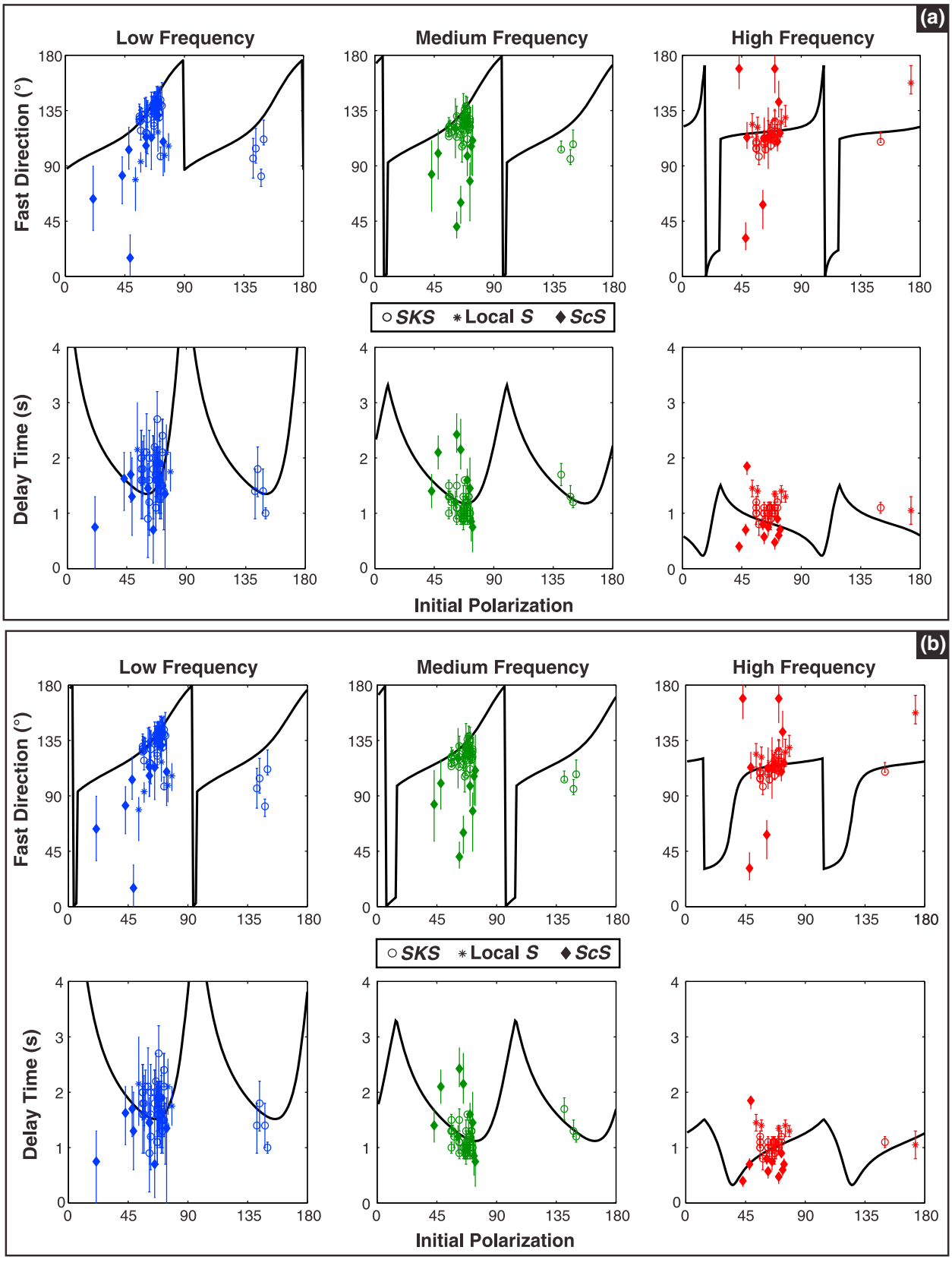
(a)
Low Frequency
Medium Frequency
High Frequency
Fast Direction (°)
Delay Time (s)
SKS
Local S
ScS
Initial Polarization
(b)
Low Frequency
Medium Frequency
High Frequency
Fast Direction (°)
Delay Time (s)
SKS
Local S
ScS
Initial Polarization

Figure 7

consistent trench-oblique to trench-parallel fast direction estimates which were interpreted in terms of a single homogeneous layer of anisotropy, most likely located within the subslab mantle [*Polet et al*., 2000; *Kaneshima and Silver*, 1995; *Russo and Silver*, 1994]. If we similarly assumed a single anisotropic layer, our full data set would yield average splitting parameters of $\phi = 135.0°$, $\delta t = 1.75$ s (standard deviation: ϕ =25.1°, $\delta t = 0.6$ s), which would be characterized as roughly parallel to the strike of the trench. It is immediately obvious, however, from the trends shown in Figure 6, that a model representing uniform anisotropy would not explain our data set well. The fact that we observe both striking variations in splitting parameters with initial polarization and a well-defined frequency dependence implies the presence of complex anisotropic structure [*Silver and Savage*, 1994; *Savage*, 1999; *Long and Silver*, 2009b].

[22] In order to assess the possibility of two or more anisotropic layers beneath Peru, we generated a series of two-layer models for all possible combinations of (ϕ, δt) for each layer using the analytical equations developed by *Silver and Savage* [1994] and making use of codes available within MSAT (MATLAB Seismic Anisotropy Toolkit) [*Walker and Wookey*, 2012]. For the purpose of this modeling exercise, we assume that *SKS*, *ScS*, and local *S* phases are sampling the same anisotropic structure, although a raypath diagram (Figure 2) indicates that the different phases may in fact be sampling different regions of the subslab mantle. We evaluated the fit between the predictions of each possible model and our splitting observations at each frequency by counting the number of splitting measurements (both ϕ and δt) out of the total data set correctly predicted by the model curve, taking into account the 95% error limits on the splitting parameter estimates. We preferred this approach to other possible measures of goodness of fit (for example, a least squares method) as it prevents outliers (particularly for measurements with similar initial polarizations but different splitting parameters estimates) from dominating the model fit. The model predictions vary with the frequency of the incoming shear wave, so the measurements were separated into the three frequency bands for testing. We tested a total of 78,336 two-layer models, varying the fast direction of each layer in 10° estimates and the delay time in 0.25 s estimates. We then queried the full set of forward models to identify the best fitting model as well as a suite of models that fit the data reasonably well.

[23] Using this procedure, we identified two best fitting two-layer models with the following parameters: upper layer $\phi = 100°$, upper layer $\delta t = 2.5$ s, lower layer $\phi = 20°$, lower layer $\delta t = 1.75$ s. The other model that fit the data equally well has the exact same ϕ parameters but with slightly larger delay times: upper layer $\delta t = 3.0$ s, lower layer $\delta t = 2.0$ s. These models both correctly predict 153 out of a total of 314 splitting parameter estimates; i.e., they fit 49% of the splitting data points (52% of the *SKS* subset, 32% of local *S*, and 32% of *ScS*, over all three frequency bands). Very similar best fitting parameters are obtained when only the *SKS* subset is used to constrain the model (upper φ: 100°, upper δt: 3 s, lower φ: 20°, lower δt: 2 s), but because the *SKS* subset is less scattered than the *ScS* and local *S* subsets, the percentage fit is higher (124 out of 236 data points, i.e., 53%). The model predictions are shown along with the splitting measurements in Figure 7a. It is impossible to fit all the data points given that often several different values of ϕ or δt were measured for the same initial polarization. However, this two-layer model does do a remarkably good job at replicating not only the strong trends with initial polarization for each frequency band but also the offset in average fast direction between different frequencies that is clearly observed for *SKS* phases in the 45°–80° initial polarization range (Figure 6c). In addition, our data points generally conform to the prediction of 90° periodicity required by two-layer models. After the top two models, the percentage fit to the data drops (the third best model fits five fewer data points) and then gradually deteriorates (the 100th best model fits 31 fewer).

[24] In order to explore the variability of models that fit the data reasonably well, the properties of the best 900 two-layer models are shown in Figures 8a–8c. The number 900 was chosen as the 900th best model fits one-third fewer data points than the best model does (102 compared to 153 data points). In Figure 8a, which compares the fast directions of each layer, the most common orientation for the lower layer is around $\phi \sim 60°$ (trench-normal) and for the upper layer around $\phi \sim 120°$ (trench-oblique to trench-parallel). There does, however, appear to be a general relationship between lower ϕ and upper ϕ, with a large difference in fast direction orientation between the two layers. (Specifically, 68% of the models included in Figures 8a–8c differ in ϕ by 50°–80°.) If the difference was exactly 90°, then splitting from the two layers would cancel each other out for the case where the layer delay times were equal. A large difference in orientation between the two layers appears to be strongly required by trends in the data (especially in the *SKS* subset). From an investigation of the model results, trends in apparent ϕ and δt with incoming polarization tend to get steeper as the angular difference between the layers increases. For Figure 8b, which illustrates common properties of the lower layer, there is a bimodal distribution, with one peak centered on $\phi \sim 40°$ (trench-normal) and delay times of 1–2 s encompassing the best model (black star) and another peak at $\phi \sim 120°$ (trench-oblique), $\delta t \sim 0.75$–1.75 s. Note that models with a lower layer oriented N-S to NNW-SSE

Figure 7. The best fitting multiple-layer models as a function of initial polarization of the incoming wave. Models plotted as black lines are based on equations from *Silver and Savage* [1994]. Shear wave splitting results and their error bars are plotted in color for comparison. Low-frequency results (0.01–0.1 Hz) are shown in blue, medium frequency (0.1–0.2 Hz) in green, and high frequency (0.2–1.0 Hz) in red. The models are also frequency dependent and were computed at 0.09, 0.15, and 0.33 Hz for the low, medium, and high-frequency bands, respectively, based on the average frequency of measurements in each band (Figure 4). (a) Best fitting two-layer model which passes through 153/314 of the data points shown (i.e., 49%). Parameters are upper ϕ: 100°, upper δt: 2.5 s, lower ϕ: 20°, lower δt: 1.75 s. (b) Best fitting three-layer model. Passes through 174/314 of the data points (55%). Parameters are upper ϕ: 100°, upper δt: 3.0 s., middle ϕ: 20°, middle δt: 2.25 s., lower ϕ: 140°, lower δt: 0.5 s.

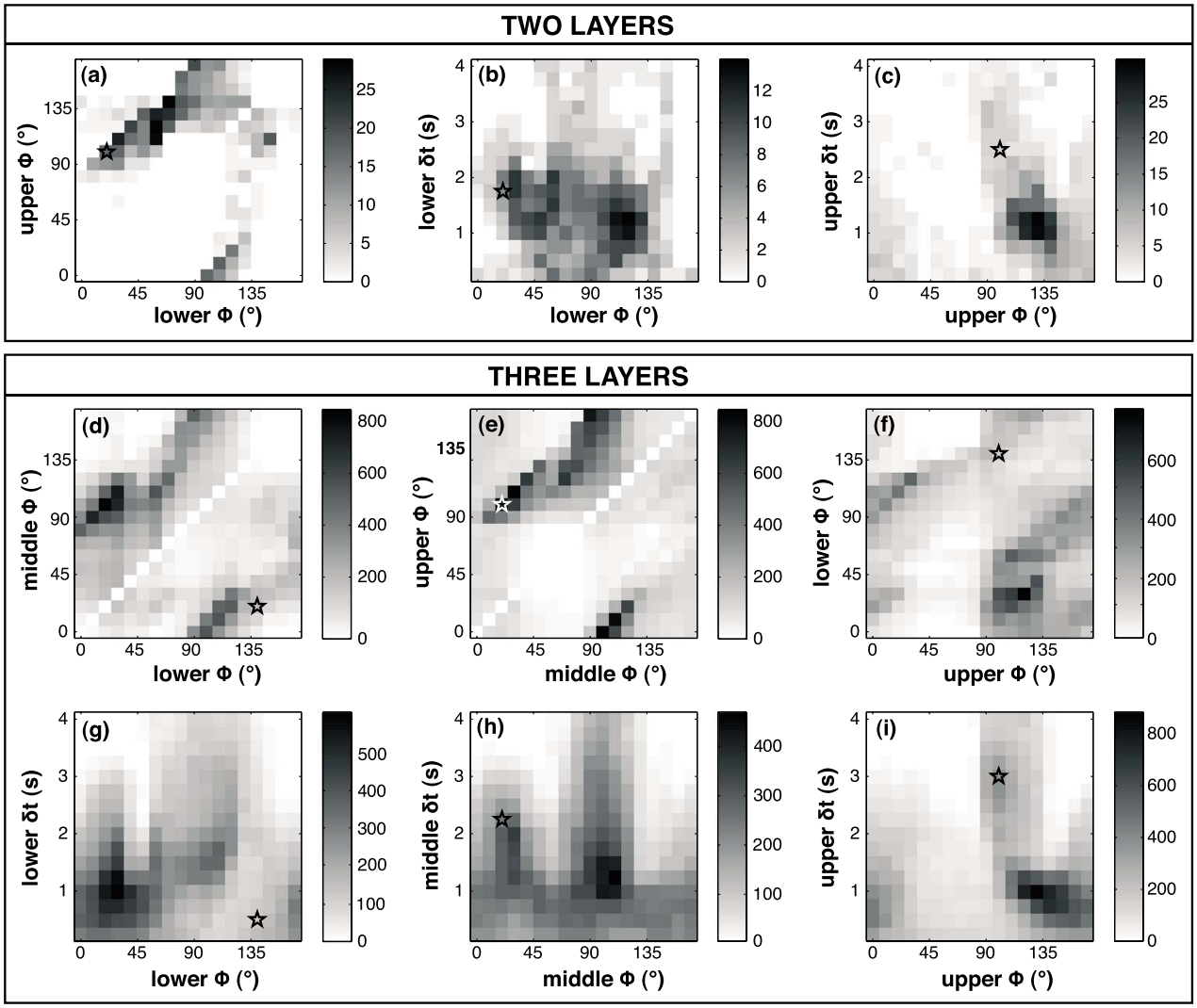

Figure 8. Characteristics of the (a–c) top 900 two-layer models and (d–i) top 45,000 three-layer models in terms of data fit, representing the properties of all the models that fit at least two thirds as many data points as the best fitting two- or three-layer model. Plots show projection of the entire model parameter space onto individual 2-D planes. Each shaded square represents a cell in the model space grid, with darker colors indicating more models with those properties. The scale bar to the right of each plot indicates the number of models for each shade of gray. The characteristics of the best fitting model are plotted with stars.

(trench-parallel) are generally inconsistent with the data. Preferred characteristics of the upper layer are focused around $\phi \sim 120°$, $\delta t \sim 1$ s (Figure 8c), which suggests a trench-oblique to trench-parallel fast direction.

[25] Given that there are (at least) three plausible candidate regions in which seismic anisotropy may reside beneath Peru (subslab mantle, slab, and overriding continental lithosphere), we extend the modeling one step further to consider three layers, using the same approach as for the two-layer modeling [*Silver and Savage*, 1994; *Walker and Wookey*, 2012]. In this case the best fitting three-layer model included an upper layer with $\phi = 100°$, $\delta t = 3.0$ s, a middle layer with $\phi = 20°$, $\delta t = 2.25$ s, and a lower layer with $\phi = 140°$, $\delta t = 0.5$ s. This geometry is identical to the best fitting two-layer model (an ESE-WNW layer over an NNE-SSW layer) but with an additional layer with modest delay time ($\delta t = 0.5$ s) placed below. This best fitting three-layer model correctly predicted 174 out of 314 data points, i.e., with 55% fit (61% of the *SKS* subset, 32% of local *S*, and 30% of *ScS*) (Figure 7b). This is an improvement by 21 data points on the best two-layer model, which fit 49% of the data set. The entirety of this improvement, however, is within the *SKS* subset; three layers fit 61% of the *SKS* results, whereas two layers fit 52%. The fit to the *ScS* and local *S* was not improved by the addition of the third layer. After the best fitting model there is a gentle decline in percentage fit (second best model fits two fewer data points, 100th best model fits 17 fewer).

[26] While the inclusion of three layers does improve the overall fit, the predicted splitting pattern for the best three-layer model is very similar to two layers, particularly in the low and medium-frequency bands (Figure 7). The main difference lies in the high-frequency band, where the three-layer model is noticeably better at replicating the trend in δt between 45° and 80°. The three-layer model is, however, equally as good as the two-layer model at replicating both the backazimuth trends and the offsets in average φ between

frequencies in the 45°–80° backazimuthal range (Figure 6c). We consider these trends to be robust features of the splitting data set that are important indicators of anisotropic heterogeneity and structure, and so in our view it is more important that a multiple-layer model reproduces these general trends rather than reproducing every point in the data set.

[27] The same two-layer substructure (an ESE-WNW layer over an NNE-SSW layer) appears to be a common characteristic of the very best models (present in 82 out of the 100 best models). In order to better constrain this two-layer substructure within the three-layer models, we examine the variability across the parameter space of models that fit the data reasonably well. In Figures 8d–8i we display properties of the top 45,000 three-layer models (only 0.2% of all the possible models), which again represent those models that fit at least two thirds as many data points as the best three-layer model (116 points compared to 174). Figures 8d and 8g demonstrate that the lowermost layer often has $\phi \sim 0°$ to 45° (NNE-SSW) and $\delta t \sim 1$ s. Likewise, the uppermost layer (Figures 8f and 8i) most commonly has $\phi \sim 90°$ to 140° (ESE-WNW) with $\delta t \sim 1$ s. The middle layer, however, has a bimodal distribution (Figures 8e and 8h), with ϕ often either around NNE-SSW (0° to 45°) or ESE-WNW (90° to 140°), both with $\delta t \sim 1$–2 s. Figure 8e shows that often when the middle layer has $\phi \sim$ NNE, then the upper layer has $\phi \sim$ ESE, and Figure 8d demonstrates that when the middle layer has $\phi \sim$ ESE, then the lower layer has $\phi \sim$ NNE. Figure 8f also shows that the most frequent combination of uppermost ϕ and lowermost ϕ is an upper layer orientated ~ ESE and a lower layer orientated ~ NNE.

[28] Overall the three-layer models seem to be reproducing a consistent two-layer substructure (very similar to the best fitting two-layer models) over and over again but with an additional third layer (either above, below, or in-between) that is poorly constrained. The results of our multiple-layer analysis, therefore, from both two-layer and three-layer modeling, indicate that there is likely an ESE-WNW oriented (trench-oblique to trench-parallel) anisotropic layer above a NNE-SSW oriented (trench-normal) anisotropic layer (although it should be kept in mind that other geometries are also a possibility). Given the improvement to fit offered by the best three-layer solution, a third anisotropic layer may also be present, but its properties cannot be constrained by our present data set. Further analysis, discussed in sections 5 and 6 below, will be required in order to confidently place each layer within the subduction zone structure. We further note that the delay times are typically quite large in the uppermost layer of our models (best two-layer model: $\delta t = 2.5$ s, best three-layer model: $\delta t = 3$ s). Assuming a 70 km thickness, this would suggest unusually strong anisotropy (20–25%), for which an obvious explanation is not readily available. We expect that future work will be able to better constrain the anisotropic properties (including the strength) of the upper layer by utilizing local *S* measurements from shallow events below the Peru Lithosphere and Slab Experiment (PULSE) deployment that has been recently situated over the southern flat-slab region [*Long et al*., 2012].

5. Source-Side Measurements

[29] Given our inference of a layer of anisotropy beneath NNA with a trench-normal fast splitting direction, underneath another layer with a trench-oblique (to subparallel) fast direction, we seek complementary measurements that place more direct constraints on anisotropy from specific components of the subduction zone. One region we are particularly interested in is the subslab mantle, as this will give us important information regarding the mantle flow field beneath the Peruvian flat slab. If the lower layer from our models originates in the subslab mantle, then this would predict trench-perpendicular mantle flow beneath the flat-slab region, where previous authors have inferred trench-parallel fast splitting directions, based on more limited data availability at NNA [*Kaneshima and Silver*, 1995; *Polet et al*., 2000; *Russo and Silver*, 1994].

[30] The best method to isolate anisotropy from the subslab component, and thus directly investigate mantle flow dynamics, is via source-side splitting measurements [e.g., *Russo and Silver*, 1994; *Russo*, 2009; *Foley and Long*, 2011; *Lynner and Long*, 2013]. We therefore measure the splitting of direct teleseismic *S* phases from events originating within the Peruvian slab recorded at distant stations (40°–80°). This distance range is chosen to exclude *S* phases that have passed through D" or that may interfere with *SKS* arrivals. We note, however, that in the 40°–60° distance range, depending on the source depth, focal mechanism, and frequency content, some contamination of the transverse components from the *SP* phase can occur; in the absence of effective quality control during splitting analysis, it is possible to misinterpret this contamination as shear wave splitting [*Tono and Fukao*, 2013]. We followed the station selection approach of *Russo and Silver* [1994], *Foley and Long* [2011], and *Lynner and Long* [2013]; specifically, we selected stations that exhibit null *SKS* splitting at a wide range of backazimuths at the frequencies under study (0.01–0.1 Hz). At these stations, direct *S* phases undergo little or no splitting in the upper mantle beneath the receiver, and so any splitting can be attributed to anisotropy near the earthquake source in Peruvian subslab mantle. We examined earthquakes originating in the Peruvian slab with magnitudes greater than 5.0 at seven previously identified null stations situated in North America (CBN, NHSC, NE80, NE75 [*Long et al*., 2010; *Foley and Long*, 2011]) and Africa (DBIC, MBO, ASCN [*Lynner and Long*, 2012, 2013]) (Figure 9). Calculations of the splitting parameters were performed using the same methodology as for the other phases (section 2.2). All direct *S* arrivals were filtered using our low-frequency band only (0.01–0.1 Hz) as this was equivalent to the frequency range at which the stations were originally classified as null using *SKS* phases.

[31] We plot the source-side splitting measurements at the earthquake location in Figure 9; fast directions are transformed from receiver-side coordinates to source-side coordinates by reflecting fast directions measured at the station across the great circle path from earthquake to receiver to correct for upgoing versus downgoing ray geometry [see, e.g., *Foley and Long*, 2011]. Due to the geometry of the subduction zone, a small fraction of the direct *S* phases have raypaths that travel through the subducting slab itself, represented by the color red in Figures 9 and 10. The majority of the direct *S* phases meanwhile, as plotted in blue, have mostly sampled the subslab mantle (Figure 10). In Figure 9 we also plot null *S* splitting measurements, which appear to be somewhat consistent with the orientation of the corresponding splits. This map demonstrates spatial differences in subslab anisotropy across the subduction zone that cannot be

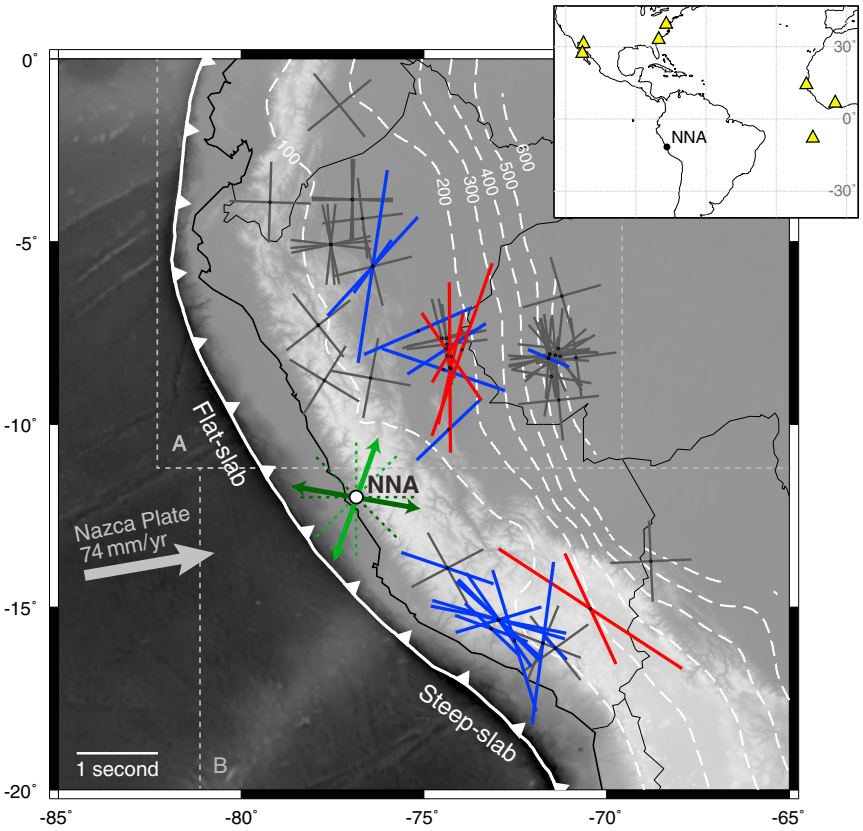

Figure 9. Map of source-side splitting results recorded at teleseismic stations (yellow triangles). Orientation of the colored line represents the measured fast direction, and the length of the line the delay time. White bar in lower left hand corner is equivalent to 1 s. Splits are positioned at the location of the source event. Red bars represent splits that have mostly sampled a steeply dipping portion of the slab (Figure 10). Blue bars, on the other hand, have mostly sampled the subslab mantle (Figure 10). Gray crosses represent null measurements and are aligned according to the possible fast/slow directions. At NNA, the light green arrows represent the lower layer and the dark green arrows the upper layer as predicted by our best two- and three-layer anisotropic models (Figure 7). The dashed green lines are limits on the orientation of the upper and lower layers inferred from the range of reasonable multiple-layer models (Figure 8). Slab contours (dashed white line) are from *Hayes et al*. [2012]. Boxes labeled A and B, outlined by gray dotted lines, represent the areas plotted in 3-D in Figure 10.

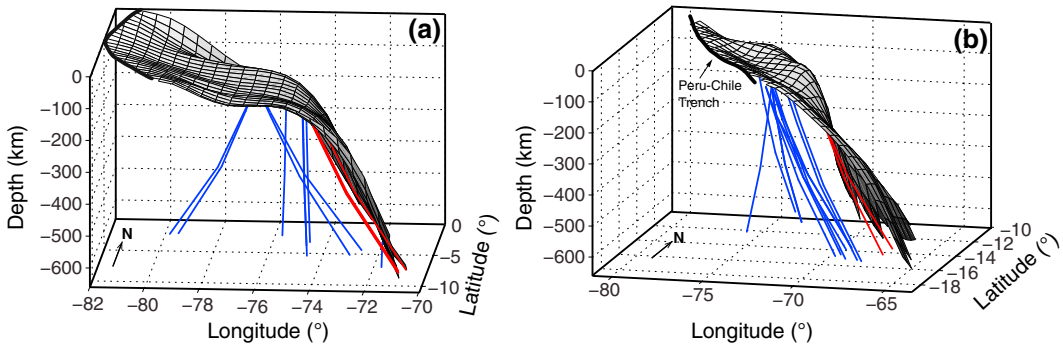

Figure 10. Three-dimensional raypaths of source-side splitting events corresponding to the results shown in Figure 9. Grey surfaces represent the inferred shape of slab based on the South American slab model of *Hayes et al*. [2012]. Blue raypaths appear to travel through the subslab mantle beneath Peru, whereas red paths appear to sample the subducting slab. (a) Geometry of the rays and flat-slab subduction in northern and central Peru. (b) Same for southern Peru where the slab is transitioning to steeper subduction.

characterized using data from station NNA alone. In the central and northern part of the flat-slab region (around 8°S, 74°W, inside box A), measurements that have been inferred to predominantly sample the subslab mantle (blue bars, eight individual measurements) show predominately trench-perpendicular (or subperpendicular) fast directions (average: $\phi = 55°$, $\delta t = 1.6$ s, standard deviation: $\phi = 33°$, $\delta t = 0.5$ s). In contrast, measurements for this region that appear to sample the dipping slab to the east (red bars, five individual measurements) show a greater tendency toward nearly trench-parallel fast orientations (average: $\phi = 5°$, $\delta t = 1.5$ s, standard deviation: $\phi = 25°$, $\delta t = 0.6$ s). A table listing all the individual splitting parameters is contained in the supporting information.

[32] Further to the east, where the slab resumes its descent into the mantle at a normal dip, we identified a large cluster of 15 null measurements (around 8°S, 71°W, see Figure 9) that originate from deep events (⩾550 km), that also cover a relatively wide range of initial polarizations (largest gap 55°). In some subduction zones (e.g., Tonga) significant source-side splitting has been identified for similarly deep events [*Foley and Long*, 2011], but our spread of null observations suggests that there is little or no contribution from anisotropy deeper than 550 km at this location. This is in agreement with the usual assumption that seismic anisotropy is concentrated in the upper mantle [e.g., *Meade et al*., 1995] and provides supporting evidence for our earlier assumption of no source-side contamination of our *ScS* measurements originating from this region. We note, however, that many of the *ScS* events used in this study originate to the south of the events used in our source-side analysis (diamond symbols ~27°S in Figure 1). No source-side measurements have yet been made in this region, and thus source-side contamination of *ScS* phases cannot be entirely ruled out. In the southern part of Peru (around 15°S, 73°W, inside box B), over the steeper subduction regime in Figure 9, the subslab measurements (12 blue bars) yield approximately trench-parallel fast orientations (average: $\phi = 128°$, $\delta t = 1.3$ s, standard deviation: $\phi = 30°$, $\delta t = 0.5$ s).

[33] Considering the distribution of fast splitting directions (and nulls) and their corresponding travel paths through the upper mantle, we infer that in the vicinity of the flat-slab segment the subslab mantle is dominated by trench-normal fast splitting directions. The slab itself also appears to be anisotropic, with fast directions that approximate trench-parallel, for raypaths that travel through the slab. This inference is generally consistent with the findings from our multiple-layer modeling efforts, which generally favor models with a layer of trench-normal fast directions below a layer that is trench-oblique to subparallel. The source-side splitting pattern does not, however, exactly replicate our inferences about anisotropy beneath NNA from our multiple-layer modeling (green arrows, Figure 9), especially for the upper layer. It is important to keep in mind that our source-side measurements are not sampling exactly the same region of the upper mantle. The multiple-layer analysis applies to the upper mantle directly beneath NNA (white dot, Figure 9), where unfortunately we did not obtain any source-side measurements.

6. Discussion

6.1. Comparison With Previous Studies

[34] A key finding from this study has been the sheer wealth of information available from the examination of shear wave splitting at just one long-running seismic station. Previous early studies at NNA, which has been operating since 1988, had just a few years' worth of data which yielded a handful of high-quality shear wave splitting measurements. *Helffrich et al*. [1994] produced six splitting measurements and *Kaneshima and Silver* [1995] just four, which were not enough to establish systematic variations in the apparent splitting parameters. *Helffrich et al*. [1994] did, however, produce a good quality *SKKS* measurement ($\phi = 107° \pm 4°$, $\delta t = 2.2\text{ s} \pm 0.35\text{ s}$) at 29° backazimuth, where our data coverage is lacking. The frequency content at which this measurement was made is unavailable, so we could not use it to directly constrain our models, but we can say that it is consistent with our best fitting two- and three-layer models in the low- and medium-frequency bands. Overall, though, the number of measurements made by previous authors is small in comparison to the size of the data set available today; in this paper we have presented results from 61 *SKS*, 12 *ScS*, and seven local *S* individual events in addition to 28 source-side measurements. This is a large data set not only in comparison to earlier work at this station but also for shear wave splitting studies in general.

[35] Such an abundant data set has given us the ability to better resolve complexities in anisotropy manifested in variations in apparent splitting with incoming polarization backazimuth, frequency dependence, and lateral sampling differences. With the detailed data set available, it has been possible to tease out variability of anisotropic structure, both laterally and with depth, in the subduction zone. Previous studies of splitting at NNA, given the small number of measurements available, usually estimated splitting parameters from stacked waveforms to provide an average for the station. Without the detailed data set available today, previous workers could only infer a single homogeneous layer of anisotropy with an effectively trench-parallel fast splitting direction. This inference was later used to support a model of trench-parallel subslab anisotropy, due to trench rollback [*Russo and Silver*, 1994]. While this model may correctly describe anisotropy elsewhere in the South American subduction system, our updated analysis does not support this interpretation beneath the Peruvian flat-slab segment.

[36] Our study therefore highlights the greater insights that can be reached by revisiting shear wave splitting at long-running seismic stations, as demonstrated by *Marson-Pidgeon and Savage* [1997, 2004] for permanent station SNZO in New Zealand. However, it also sounds a note of caution for splitting studies based solely on limited data sets or temporary deployments. In particular, and as pointed out by many other authors, caution is advisable when presenting stacked or average splitting parameter estimates, and analysts must be aware of the limitations of their data sets when interpreting such results. Particularly in complex tectonic settings such as a subduction zone, complexities in anisotropic structure may very well be present even if they cannot be resolved with the data available. Without the full picture available from a detailed, thorough shear wave splitting investigation, interpretations in terms of mantle processes can easily be incorrect even in their first-order aspects. Perhaps the best possible scenario is when temporary deployments, which are usually more abundant and thus provide valuable spatial coverage, can be combined with longer running permanent stations like NNA that can capture a higher degree of anisotropic complexity.

6.2. Frequency Dependence

[37] To date there have been a few other published studies of frequency dependence of splitting parameters in subduction zone settings [*Marson-Pidgeon and Savage*, 1997, 2004; *Fouch and Fischer*, 1998; *Greve et al*., 2008; *Wirth and Long*, 2010]. Several different models have been proposed to explain this observed frequency dependence. Broadly, these models can be divided into two categories: those that invoke changes in anisotropic geometry with depth (extension of multiple layers) [*Silver and Savage*, 1994; *Fouch and Fischer*, 1998; *Rümpker and Silver*, 1998; *Saltzer et al*., 2000; *Wirth and Long*, 2010] and those that invoke small-scale heterogeneities (i.e., when anisotropic properties vary over a distance smaller than the lowest frequency Fresnel zone [*Marson-Pidgeon and Savage*, 1997; *Greve et al*., 2008; *Wirth and Long*, 2010]). The frequency effect for depth-dependent anisotropy has been investigated by a few studies but is still debated. We do know that the patterns predicted by the multiple-layer analysis in this study using the formulation of *Silver and Savage* [1994] are dependent on the period of the incoming shear wave. *Saltzer et al.* [2000] carried out a theoretical study of multiple-layer anisotropy and argued that, according to Fréchet kernels calculated using perturbation theory, in general lower frequency measurements should be more sensitive to the upper (near-surface) layers. *Chevrot and Monteiller* [2009], however, disagree that there is a simple relationship between frequency and the depth of anisotropy for complex Earth models and argue instead that the coherence of fabrics and the location of heterogeneities will control the nature of frequency dependence.

[38] For the case of small-scale heterogeneities, if anisotropy varies over a distance smaller than the lowest frequency Fresnel zone of the waves (that is, the region of greatest sensitivity to anisotropic structure), then frequency dependence can occur. These small-scale heterogeneities can be randomly distributed [e.g., *Wirth and Long*, 2010] or take the form of aligned melt bands or fractures in the shallow crust, which have a SPO (shape preferred orientation) type effect [e.g., *Greve et al*., 2008]. In either case frequency-dependent splitting can be generated, as shear waves with higher frequency content will possess narrower Fresnel zones and will sample smaller, localized pockets of coherent anisotropy within the medium, whereas shear waves with lower frequency content will possess wider Fresnel zones that average out any smaller scale variability in elastic properties, thus resulting in bulk effective anisotropy. If a lateral step change in anisotropy occurs within the sensitivity range (Fresnel zone), then synthetic tests indicate that splitting parameters will show a 180° periodicity with initial polarization [*Rümpker and Ryberg*, 2000]. The inherent scale length of any heterogeneity is therefore important. Following the calculation for a Fresnel zone from *Gudmundsson* [1996], we calculate that our low-frequency band (0.01–0.1 Hz) would have a Fresnel zone width on the order of ~100 km at lithospheric depths or approximately tens of kilometers at crustal depths. Any heterogeneities present at such depths would therefore need to be smaller than the width of these Fresnel zones in order to produce any frequency dependence.

[39] It is not possible to exclude any of the potential explanations for frequency dependence for our data set. However, an SPO type mechanism from melt inclusions seems less likely in our study region, given that there is no volcanic activity at the surface above the flat-slab segment, so there is little reason to expect bands of partial melt. Pockets of melt that are now frozen into the crust left over from past episodes of volcanism, however, could still be a possibility. Instead, it seems more plausible to infer that the frequency dependence results from heterogeneity in anisotropic structure, most likely with depth but perhaps also laterally (i.e., small-scale anisotropic heterogeneities). Given the success of our multiple-layer models in predicting a trend of frequency dependence similar to that observed in our data, it would appear likely that depth-varying anisotropy beneath NNA is the source of the frequency dependence observed in our data.

6.3. Limitations of Multiple-Layer Models

[40] We have shown that multiple layers of anisotropy beneath NNA can replicate both the observed frequency dependence and robust trends in apparent splitting parameters with respect to initial polarization present in our data set, especially in the *SKS* subset. It should be kept in mind, however, that other possible explanations for these observations may exist. For example, dipping layers of anisotropy, which we have not considered in our modeling, could also generate variability with incoming polarization/backazimuth. In terms of the observed frequency dependence, this could also be generated by small-scale heterogeneities, as discussed in the previous section, but we currently do not have any direct evidence of what processes might produce such heterogeneities beneath the Peruvian flat slab.

[41] An important caveat of the multiple-layer models is that they do not reproduce all of the variation in the data; the best fitting two-layer model satisfies only 49% of the measurements, while the best fitting three-layer model fits 55% of the observations. The majority of the misfit originates from the discrepancy between splitting parameters (especially ϕ) from different phases with the same initial polarization (Figure 6). Large discrepancies are impossible to match with multiple layers as only one value of ϕ and one value of δt are predicted at any given initial polarization. There are several possible reasons why measurements from different phases might not agree. First, there could be errors in estimating the initial polarizations of the local *S* and *ScS* events from the waveform. Comparison with independent predictions of initial polarization from the focal mechanisms, however, demonstrated for our data set that this error is less than 25° and usually less than ~10° (Figure 3). Second, the average dominant frequency of each phase differs slightly within each frequency band but most noticeably in the high-frequency band (0.2–1.0 Hz) (Figure 4). Different frequency content will therefore generate different frequency dependence in the splitting parameters. As mentioned previously in section 3, this can explain the apparent discrepancy in delay times between the local *S*, *SKS*, and *ScS* high-frequency results in Figure 6d (red symbols), with the higher frequency phases producing smaller delay times, but it is less clear how such an effect could account for the large variability within the fast directions, particularly in the medium- and low-frequency bands (Figure 6c).

[42] Third, and perhaps most likely, there may be an effect due to the different raypaths traveled by the different phases contained in our data set. This could affect the shear wave splitting parameters obtained in two different ways. The variability of backazimuths and incidence angles could alter the

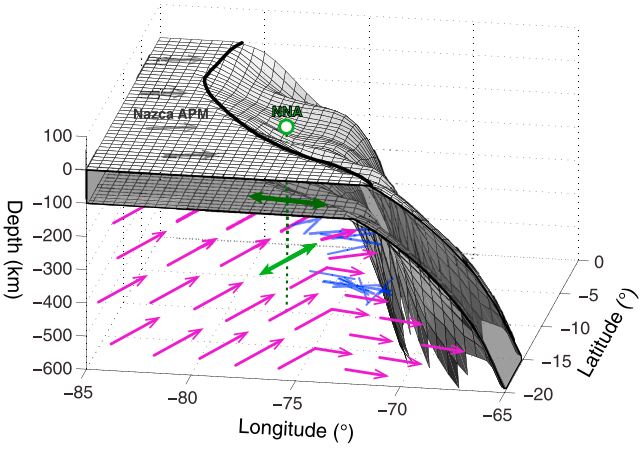

Figure 11. Schematic interpretation of mantle flow (magenta arrows) beneath the subducting slab based on source-side splitting measurements from phases that mainly passed through the subslab mantle (blue bars, same as Figure 10, plotted at 400 km depth) and the results of multiple-layer analysis at NNA (green arrows show the orientation of the fast directions for the best two-layer model from Figure 7a). Gray arrows point in the direction of absolute plate motion (APM) [*Gripp and Gordon*, 2002].

angle between the anisotropy symmetry axis and the raypath, thus generating variable splitting parameters. Given that both *SKS* and *ScS* arrive with small incidence angles (<10°), however, this effect is likely minimal. For the local/direct *S*, however, the incidence angles are larger (~30°), and differences in raypath thus could play a bigger role. Another consideration is that the spatially different travel paths of *SKS*, *ScS*, and local *S* means that they sample different subregions of anisotropy within the subduction zone. The raypath diagram in Figure 2 reveals that *SKS* phases arrive mostly from the west at the station with near vertical incidence and sample the region near the trench where the slab is beginning to flatten. *ScS* phases also arrive at the station with near vertical incidence but generally arrive from the east. (It is also possible that the *ScS* measurements are affected by anisotropy near their source, but a major effect from source-side anisotropy is unlikely given that we only chose events deeper than 500 km.) Local *S* phases, on the other hand, arrive at the station with a shallower incidence angle from the east and generally sample much more of the mantle that lies directly beneath the flat slab. Given that the raypaths of each phase diverge most significantly in the deeper parts of the system, this would suggest that any spatial variations in anisotropy are more likely to exist in the subslab mantle. Results from our source-side investigation, from events that mostly sample subslab mantle material, do lend some support to this possibility, with variability in source-side splitting results seen at different locations in the subduction zone (Figure 9).

6.4. Implications for Subduction Zone Dynamics

6.4.1. The Subslab Mantle Flow Field

[43] Our inference from source-side shear wave splitting is that the subslab mantle beneath the flat slab likely exhibits approximately trench-normal fast splitting directions. This agrees well with a lower layer of anisotropy, with trench-normal ϕ, as predicted by the majority of our best fitting multiple-layer models at NNA. Meanwhile, beneath the normally dipping slab in southern Peru, trench-parallel to trench-oblique fast directions are seen to dominate the subslab source-side splitting patterns. Anisotropy in the subslab mantle is likely controlled by olivine LPO; based on the likely conditions of deformation in this region, E- or C-type fabrics are expected [*Karato et al.*, 2008]. Both these LPO fabrics suggest that the fast splitting direction should have the same orientation as the maximum shear direction and would thus be aligned parallel to (horizontal) mantle flow (if there is a vertical gradient in flow velocity and assuming no dependence on incidence angle or backazimuth of the ray). This simple relationship would suggest that mantle flow under the flat-slab region is normal to the trench—that is, in the same direction as the downgoing plate—but (sub-) parallel to the trench under the more steeply dipping region to the south. A sketch of this interpretation for subslab mantle flow and the observations that constrain it are shown in Figure 11.

[44] For South America, a long held notion to explain observations of trench-parallel fast splitting directions has been that retrograde migration of the Peru-Chile Trench (along with a partial barrier to flow at depth and inefficient mechanical coupling between the slab and the subslab mantle) would act to force mantle material to the side behind the retreating slab, resulting in dominantly trench-parallel flow in the subslab mantle [e.g., *Russo and Silver*, 1994] (Figure 12a). The model of *Russo and Silver* [1994], however, did not take into account variations in slab dip beneath South America, and our inference of likely trench-perpendicular subslab flow beneath the Peruvian flat-slab segment is not consistent with the general prediction of trench-parallel flow. An alternative to the model of *Russo and Silver* [1994] is the classical model of simple 2-D entrained mantle flow due to viscous coupling between the slab and the subjacent mantle that follows the subducting plate [e.g., *Hicks et al.*, 2012]. This model would be consistent with our observations for the flat-slab region but not for the steeper subduction region just to the south.

[45] The dilemma of explaining both trench-parallel and trench-perpendicular subslab fast splitting directions is not unique to Peru. On the global scale the subslab anisotropy pattern appears to be dominated by trench-parallel fast directions [*Long and Silver*, 2008, 2009a]. There are notable exceptions, however, such as Cascadia [*Currie et al.*, 2004; *Eakin et al.*, 2010], Alaska [*Christensen and Abers*, 2010; *Hanna and Long*, 2012], and the Chilean flat slab [*Anderson et al.*, 2004], which also display trench-perpendicular φ beneath the slabs similar to what we observed beneath the Peruvian flat slab. These regional exceptions are all occurring beneath slabs with relatively shallow dips, as noted by *Long and Silver* [2009] and *Song and Kawakatsu* [2012]. The correlation with slab dip suggests that the subslab mantle flow field may be influenced by a combination of the 3-D kinematics and the morphology of the subducting slab. The effect of complex slab morphology (e.g., along strike variations in dip and curvature) on the 3-D subduction flow field has been explored by *Kneller and van Keken* [2007, 2008], although their focus is only on the mantle wedge.

[46] A possible scenario that may explain these observations is that where slabs are steeply dipping they can exert a component of force (normal to the slab surface) from slab

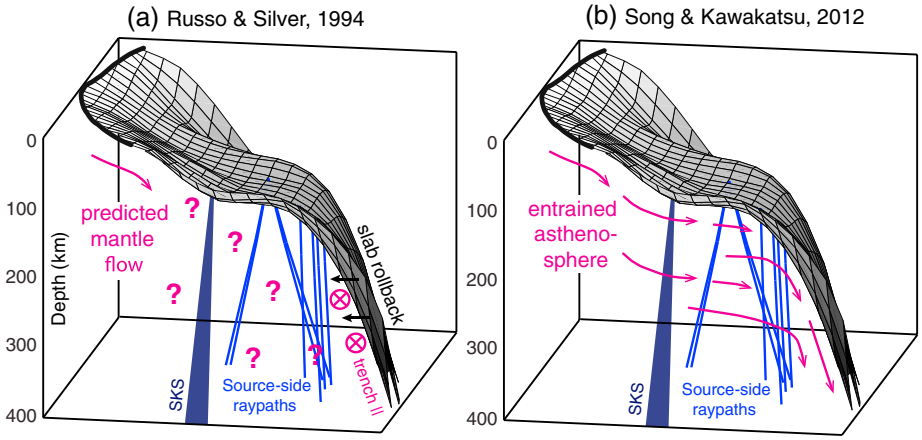

Figure 12. Schematic 3-D diagrams illustrating two hypotheses of subslab anisotropy in application to the geometry of the Peruvian flat-slab segment and the associated raypaths that traverse it. (a) *Russo and Silver* [1994]. The slab and underlying asthenosphere are uncoupled. Slab rollback pushes back on the mantle behind, squeezing out material along strike and thus setting up trench-parallel flow. Where the slab is flat, however, the prediction for the pattern of mantle flow is unclear. Magenta crosses enclosed by circles indicate asthenospheric flow that is either into or out of the page. (b) *Song and Kawakatsu* [2012]. The oceanic asthenosphere is coupled to and dragged down with the subducting slab. This asthenosphere is thought to have an effective orthorhombic symmetry, which produces variable splitting patterns depending on the dip of the subducted material, and the inclination and/or backazimuth of the rays that traverse it (Figure 13).

rollback that can induce toroidal flow and produce trench-parallel anisotropy directly beneath the slab; where subduction is shallow or flat, as under Peru, then slab rollback is likely less efficient at generating toroidal flow. This conceptual model, synthesized in cartoon form in Figure 12a, is consistent with recent numerical modeling results by *Paczkowski* [2012], who demonstrated that shallowly dipping slabs are much less efficient than steeply dipping slabs at generating trench-parallel subslab flow. These kinematic-dynamic subduction models investigated the interaction between slabs and the background flow field; *Paczkowski* [2012] found that steep slabs deflect subslab mantle flow in a nearly trench-parallel direction for the case with efficient mechanical decoupling between the slab and the subjacent mantle, but shallowly dipping slabs generally do not. The physical mechanism for possible mechanical decoupling between the slab and the subslab mantle remains poorly understood, but several possibilities were discussed in detail by *Long and Silver* [2009a], including the entrainment of a thin layer of highly deformed asthenosphere which serves as a weak decoupling zone, the presence of melt or volatiles directly beneath the oceanic lithosphere, nonlinear mantle rheology, or mechanical anisotropy.

[47] An alternative model, recently advanced by *Song and Kawakatsu* [2012] (Figure 12b), invokes 2-D flow kinematics along with anisotropy symmetry and slab morphology. They proposed that the asthenospheric upper mantle beneath ocean basins generally possesses anisotropy with orthorhombic symmetry and that a layer of asthenosphere is generally entrained beneath subducting slabs. Specifically, in the oceanic asthenosphere a combination of azimuthal anisotropy [e.g., *Maggi et al*., 2006] and radial anisotropy [$V_{SH} > V_{SV}$; *Gung et al*., 2003; *Nettles and Dziewonski*, 2008] may result in an effective orthorhombic symmetry. This model predicts fast splitting directions beneath subducting slabs that vary depending on the dip of the subduction zone, as well as the incidence angle and backazimuth of the incoming shear wave (Figure 13). In general, for vertically incident raypaths (<10°, e.g., *SKS*), shallowly dipping slabs produce trench-normal fast splitting directions, while steeply dipping slabs give trench-parallel fast directions [*Song and Kawakatsu*, 2012]. For larger incidence angles, however (e.g., those associated with our source-side splitting measurements), the splitting pattern becomes much more variable and dependent on the backazimuth.

[48] In Figures 13a and 13b we compare our source-side splitting measurements with long path lengths in the subslab mantle (shown in blue in Figures 9 and 10) to the shear wave splitting pattern predicted by *Song and Kawakatsu* [2012] for both the flat slab (region A in Figures 9 and 10) and the steeper normal subduction zone further south (region B). Measurements inferred to have raypaths that mostly travel through the slab (shown in red in Figures 9 and 10) are excluded from this comparison, given that the *Song and Kawakatsu* [2012] model does not apply to anisotropy within subducted oceanic lithosphere. For the steeper slab (Figure 13b), the majority of our source-side results (10 out of 12 blue bars) appear fairly similar to the model predictions (red bars) at both ~350° and ~75° azimuths. For the flat slab, however (Figure 13a), the model prediction appears different from most of our results (seven out of eight measurements) at three different azimuth locations (320°, 350°, 60°).

[49] We also provide a comparison between the predictions of the *Song and Kawakatsu* [2012] model and our observations of *SKS*, *ScS*, and direct local *S* splitting at NNA (Figures 13c–13e). The model, which invokes a single layer of anisotropy beneath the subducting slab and neither explicitly includes nor rules out anisotropy elsewhere in the subduction system, appears to match the NNA measurements better at higher frequencies, but unlike our preferred multiple-layer models (Figure 7), the *Song and Kawakatsu* [2012] predictions do not account for the observed frequency dependence in the splitting parameters.

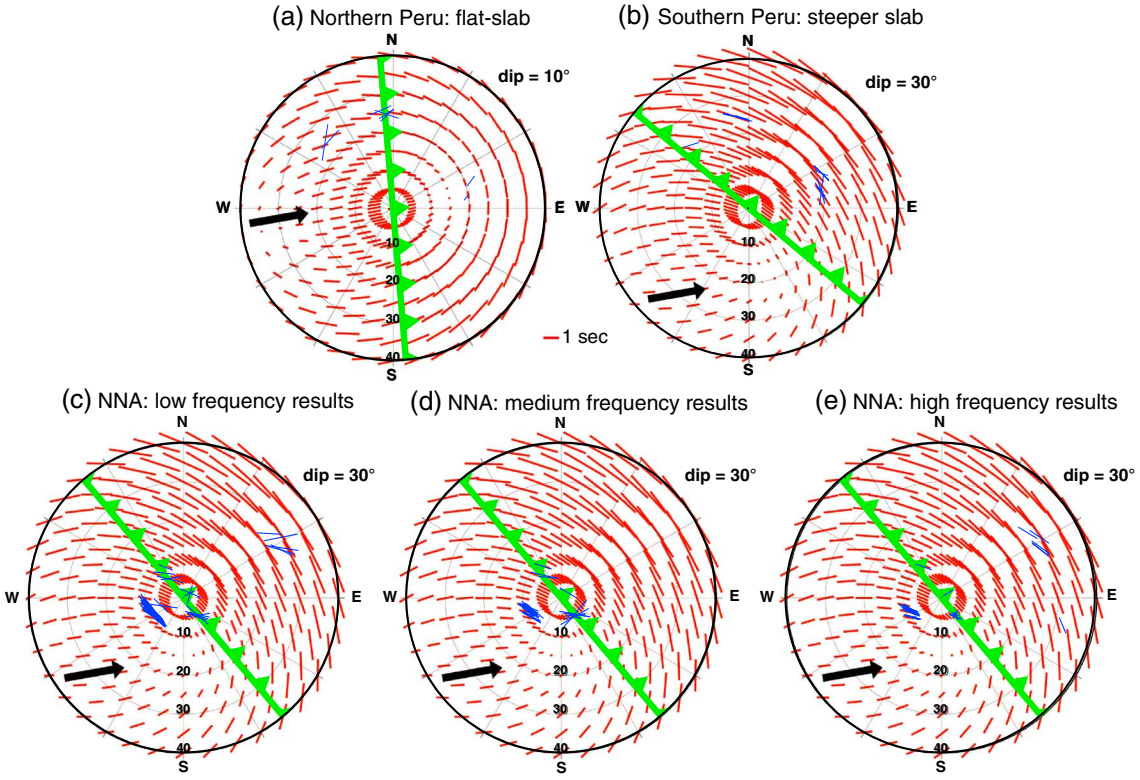

Figure 13. Stereoplots comparing the predicted shear wave splitting pattern from the *Song and Kawakatsu* [2012] model (red bars) and our shear wave splitting measurements (blue bars) for (a, b) both subslab source-side results and (c–e) *SKS*, *ScS*, and local *S* results at station NNA. The orientation and length of the bars represent fast direction and delay time and are plotted for a range of incidence angles (0°–40°) and azimuths (0°–360°). The thick green line represents the local strike of the trench and/or slab. The thick black arrow shows absolute plate motion direction [*Gripp and Gordon*, 2002]. Model predictions are for a 200 km thick layer following *Song and Kawakatsu* [2013]. (Figure 13a) Predicted and observed splitting over the flat-slab region (dip ~ 10°) in northern Peru. Includes all blue subslab measurements originating from the flat slab enclosed in area A from Figures 9 and 10. (Figure 13b) The same for southern Peru where the slab is transitioning to steeper subduction (dip ~ 30°), covering area B in Figures 9 and 10. (Figure 13c) Predicted and observed splitting for NNA recorded in the low-frequency band (0.01–0.1 Hz). (Figure 13d) The same as for Figure 13c but for the medium-frequency band (0.1–0.2 Hz). (Figure 13e) High-frequency band (0.2–1.0 Hz). Note that model predictions are independent of frequency and are therefore the same across Figures 13c–13e.

In addition, the *Song and Kawakatsu* [2012] model does not predict significant backazimuth variability for incidence angles $< 10°$ (e.g., *SKS* and *ScS*), behavior that is both observed in the data and predicted by the multiple-layer models (Figure 7). For example, differences in the measured fast polarizations between the SE, SW, and NW quadrants are not predicted by the model of *Song and Kawakatsu* [2012] (Figures 13c–13e), nor is the systematic rotation in ϕ within the SW quadrant (as is apparent in Figures 6c and 7). In any case, it is important to remember that the *Song and Kawakatsu* [2012] model does not explicitly include multiple layers of anisotropy; if multiple layers of anisotropy are in fact present beneath NNA, as indicated by the strong backazimuthal dependence and frequency dependence we observe, then a simple comparison between the (single-layer) model predictions and the observations is not straightforward.

[50] Given these observations, which model do we prefer as an explanation for our observations of subslab anisotropy beneath Peru? The *Song and Kawakatsu* [2012] model provides an elegant and simple explanation for the trench-perpendicular subslab splitting beneath NNA, while the trench-parallel subslab flow model [*Russo and Silver*, 1994; *Long and Silver*, 2008] does not explicitly take into account the complex morphology of a flat-slab segment (i.e., its varying dip and geometry) and does not make a clear prediction for what one might expect in the subslab mantle beneath the flat slab. The predictions of both models, however, seemingly contradict our subslab source-side splitting observations from northern Peru, beneath the flat-slab region (blue bars in region A of Figure 9 and blue paths in Figures 10 and 12). *Russo and Silver* [1994] predict trench-parallel ϕ under these conditions when we see trench-normal ϕ, while *Song and Kawakatsu* [2012] predict a variable azimuth-dependent splitting pattern that generally does not agree with the properties of our individual measurements (Figure 13a). There is some support from numerical models [*Paczkowski*, 2012] for the idea that even if the *Russo and Silver* [1994] model of trench-parallel flow beneath subducting slabs

induced by trench migration is generally correct, shallowly dipping slabs may not generate much trench-parallel flow. No such modeling studies incorporating a complex slab geometry specific to Peru have been run, however, and our current data set cannot discriminate between the predictions of the two different models for subslab anisotropy beneath Peru. We suggest, however, that combining the insights presented here about complex anisotropic structure beneath NNA with future work such as the analysis of ongoing dense deployments in Peru, the continued refinement of source-side splitting data sets for South America, and the implementation of numerical models with a geometry appropriate to the Peru subduction system will better elucidate the actual mechanism for the observed anisotropy.

6.4.2. Anisotropy in the Subducting Plate and Overriding Continent

[51] A lower layer of trench-normal anisotropy, as predicted by our best fitting multiple-layer models, correlates well with fast splitting directions inferred from subslab source-side measurements beneath the Peruvian flat slab. An upper layer of trench-oblique to subparallel (ESE-WNW) anisotropy is also frequently predicted by our best fitting multiple-layer models, but the depth of such a layer is less easy to pinpoint. We consider two likely sources: the subducting slab and the overriding continental plate.

[52] For the subducting Nazca plate, we have supporting evidence for source-side splitting due to anisotropy within the slab with approximately N-S (trench-subparallel) fast splitting directions (red paths in Figure 10b). If the upper layer of anisotropy from our multiple-layer models beneath NNA indeed corresponds to the subducting slab, and assuming anisotropy throughout the subducting slab is uniform, then we would require a mechanism to reconcile an ESE-NNW fast direction beneath NNA with N-S fast direction recorded by direct teleseismic *S* waves that travel through the dipping portion of the slab. In terms of deformation fabrics for the oceanic lithosphere, any anisotropy signal is likely dominated by either A- or D-type olivine LPO; for either scenario, the fast axes should align parallel to the maximum shear direction [*Karato et al*., 2008]. Globally oceanic lithosphere has been typically found to have anisotropic fast directions parallel to the paleo-spreading direction [e.g., *Hess*, 1964; *Francis*, 1969; *Montagner and Tanimoto*, 1991; *Maggi et al*., 2006]. It is thought that anisotropic fabric is "frozen in" as the lithosphere progressively cools and thickens, and this signal of anisotropy may be preserved in subducting slabs [e.g., *Song and Kim*, 2012; *Audet*, 2013]. This simple model of lithospheric anisotropy frozen in at the ridge would predict trench-perpendicular fast splitting directions in the downgoing Nazca plate and thus a trench-perpendicular layer in the flat slab beneath NNA. This would be inconsistent with the upper layer of trench-oblique anisotropy from our multiple-layer modeling and also likely inconsistent with the trench-subparallel fast orientations from the dipping slab, although the dipping nature of the anisotropy needs to be taken into consideration.

[53] An alternative mechanism for generating anisotropy in the subducting slab is the alignment of serpentinized vertical cracks that produce a combined SPO and LPO effective anisotropy [*Faccenda et al*., 2008; *Healy et al*., 2009]. For vertically propagating shear waves passing through a dipping slab, this model would predict trench-parallel fast directions. This could potentially explain an upper layer with a trench-subparallel fast direction in the slab beneath NNA. However, the *Faccenda et al*. [2008] model cannot explain the source-side splitting we observe for direct teleseismic *S* raypaths, located around 200 km depth, that travel through the dipping portion of the slab (Figure 10b). Such a ray geometry would produce no observable shear wave splitting for the aligned cracks model unless the geometry of the cracks was substantially different (i.e., parallel to the slab plane) from that predicted by *Faccenda et al*. [2008] and *Healy et al*. [2009] (i.e., vertical cracks) and would also require the stability of hydrous phases below 200 km depth. Overall, our data set is not able to distinguish the full geometry of anisotropy in the subducting slab, and its source remains unclear.

[54] The other possibility is that the upper layer of anisotropy beneath NNA inferred from our multiple-layer modeling actually corresponds to the overriding continental plate. The World Stress Map [*Heidbach et al*., 2008] shows that many of the maximum horizontal compressive stress indicators in southern Peru are E-W to SE-NW, very similar to the fast direction in our upper model layer (ESE-NNW, i.e., trench-oblique). Anisotropy with this geometry could be potentially generated within the continental South American plate by two different methods: the first would be pure shear deformation of the lower continental crust or upper lithospheric mantle, producing fast splitting directions perpendicular to shortening. The second possibility would be in the shallow continental crust from stress-aligned cracks/fractures [e.g., *Crampin*, 1994]. This would generate SPO type anisotropy with a fast direction parallel to the horizontal compressive stress orientation. Such crack-induced anisotropy is only thought to be viable, however, for the upper 10–15 km of the crust and would therefore only generate small delay times (< 0.3 s) [*Savage*, 1999].

[55] Overall, we cannot constrain whether anisotropy is present or not within the continental crust or lithosphere beneath NNA, but we note that the local stress regime is consistent with the upper layer of anisotropy predicted by our multiple-layer modeling. In contrast, we do have some evidence for anisotropy within the subducting slab, from source-side observations that sample dipping slab material, but we do not know yet of a satisfactory mechanism to explain trench-subparallel splitting in the slab. Future work on spatially dense splitting data sets that have seismic stations further inland will hopefully incorporate many more local *S* events, especially those occurring shallow part of the flat slab. This will help to characterize anisotropic signals from different components of the subduction zone. In combination with the application of other techniques such as anisotropic receiver function analysis [e.g, *Nikulin et al*., 2009; *Song and Kim*, 2012; *Wirth and Long*, 2012], this future work should shed more light on the anisotropic structure of the Peruvian slab and overlying South American continent.

7. Summary

[56] We have investigated shear wave splitting from 20+ years of available data at permanent station NNA as well as source-side splitting from earthquakes originating in the Peruvian slab. Our data analysis has revealed frequency-dependent shear wave splitting, strong trends in apparent splitting parameters with backazimuth/polarization, and lateral variations that are all consistent with the presence of complex

anisotropic structure. We infer that the anisotropic geometry in the subslab mantle likely has a trench-normal fast orientation beneath the flat-slab segment, with a trench-oblique fast direction beneath the normally dipping slab in southern Peru. We also find evidence for a shallower layer of anisotropy with trench-oblique to trench-subparallel fast direction beneath station NNA, which may correspond to anisotropy within the subducting slab and/or in the overriding plate. Based on the constraints on subslab anisotropy provided by our data set, we suggest that the pattern of mantle flow appears to be different beneath the flat-slab region and the adjacent normally dipping slab region. This suggests that subslab mantle flow may play an important role in the origin and evolution of flat-slab systems, but more work is needed to understand what this role might be.

[57] The feedbacks between slab morphology and ambient mantle flow beneath Peru, as well as in subduction systems more generally, still remain to be elucidated in full, but we expect that future investigations from both an observational and geodynamic modeling point of view will yield progress on this important problem. Specifically, future work to map the mantle flow patterns in the vicinity of flat slabs in more spatial detail is needed. Ongoing seismic deployments in flat-slab regions, particularly the Peru Lithosphere and Slab Experiment (PULSE) that was recently deployed above the Peruvian flat slab [*Long et al*., 2012], will provide unprecedented spatial coverage of flat-slab settings. The implementation of analysis techniques that can place tighter constraints on the depth distribution of anisotropy, such as anisotropic receiver function analysis, will also help to further constrain models for anisotropic structure beneath Peru. Inferences of the mantle flow field from seismic anisotropy in subduction systems with a flat-slab morphology represent an important benchmark for conceptual and geodynamic models of flat-slab formation and evolution and may help to resolve the many unanswered questions related to the geodynamics of flat-slab subduction.

[58] **Acknowledgments.** Data used in this study come from the Global Seismographic Network, Global Telemetered Seismograph Network, Geoscope, United States National Seismic Network, NARS array, and Caltech Regional Seismic Network and were accessed via the Data Management System (DMS) of the Incorporated Research Institutions for Seismology (IRIS). We are grateful to collaborators on the Peru Lithosphere and Slab Experiment (PULSE), particularly Susan Beck and Lara Wagner, for helpful discussions on Peru flat-slab dynamics. We also thank Martha Savage, Teh-Ru Alex Song, and an anonymous reviewer for suggestions that helped improve the manuscript. We are grateful to Teh-Ru Alex Song for providing the model predictions shown in Figure 13. We acknowledge support from Yale University and from NSF via grants EAR-0911286 and EAR-0943962.

References

Aleman, A. M. (2006), The Peruvian flat-slab. Backbone of the Americas, Asociacion Geologica Argentina, *Geological Society of America Symposium*, Abstract with Programs, 17, Mendoza.

Anderson, M. L., G. Zandt, E. Triep, M. Fouch, and S. Beck (2004), Anisotropy and mantle flow in the Chile-Argentina subduction zone from shear wave splitting analysis, *Geophys. Res. Lett.*, *31*, L23608, doi:10.1029/2004GL020906.

Audet, P. (2013), Seismic anisotropy of subducting oceanic uppermost mantle from fossil spreading, *Geophys. Res. Lett.*, *40*, 173–177, doi:10.1029/2012GL054328.

Bowman, J. R., and M. Ando (1987), Shear-wave splitting in the upper-mantle wedge above the Tonga subduction zone, *Geophys. J. R. astr. Soc.*, *88*, 25–41.

Cahill, T., and B. L. Isacks (1992), Seismicity and shape of the subducted Nazca Plate, *J. Geophys. Res.*, *97*(B12), 17,503–17,529.

Chevrot, S., and V. Monteiller (2009), Principles of vectorial tomography—The effects of model parameterization and regularization in tomographic imaging of seismic anisotropy, *Geophys. J. Int.*, *179*, 1726–1736.

Christensen, D. H., and G. A. Abers (2010), Seismic anisotropy under central Alaska from *SKS* splitting observations, *J. Geophys. Res.*, *115*, B04315, doi:10.1029/2009JB006712.

Crampin, S. (1994), The fracture criticality of crustal rocks, *Geophys. J. Int.*, *118*, 428–438.

Crotwell, H. P., T. J. Owens, and J. Ritsema (1999), The TauP ToolKit: Flexible seismic travel-time and raypath utilities, *Seismol. Res. Lett.*, *70*, 154–160.

Currie, C. A., J. F. Cassidy, R. D. Hyndman, and M. G. Bostock (2004), Shear wave anisotropy beneath the Cascadia subduction zone and western North America craton, *Geophys. J. Int.*, *157*, 341–353.

Eakin, C. M., M. Obrebski, R. M. Allen, D. C. Boyarko, M. R. Brudinski, and R. Porritt (2010), Seismic anisotropy beneath Cascadia and the Mendocino triple junction: Interaction of the subducting slab with mantle flow, *Earth Planet. Sci. Lett.*, *297*, 627–632.

Faccenda, M., L. Burlini, T. V. Gerya, and D. Mainprice (2008), Fault-induced seismic anisotropy by hydration in subducting oceanic plates, *Nature*, *455*, 1097–1110.

Foley, B. J., and M. D. Long (2011), Upper and mid-mantle anisotropy beneath the Tonga slab. *Geophys. Res. Lett.*, *38*, L02303, doi:10.1029/2010GL046021.

Fouch, M. J., and K. M. Fischer (1998), Shear wave anisotropy in the Mariana subduction zone, *Geophys. Res. Lett.*, *25*, 1221–1224.

Francis, T. J. G. (1969), Generation of seismic anisotropy in the upper mantle along the mid-oceanic ridges, *Nature*, *221*, 162–165.

Gaherty, G. B., and T. H. Jordan (1995), Lehmann discontinuity as the base of an anisotropic layer beneath continents, *Science*, *268*, 1468–1471.

Greve, S. M., M. K. Savage, and S. D. Hofmann (2008), Strong variations in seismic anisotropy across the Hikurangi subduction zone, North Island, New Zealand, *Tectonophysics*, *462*, 7–21.

Gripp, A. E., and R. G. Gordon (2002), Young tracks of hotspots and current plate velocities, *Geophys. J. Int.*, *150*, 321–361.

Gudmundsson, O. (1996), On the effect of diffraction on traveltime measurements, *Geophys. J. Int.*, *124*, 304–314.

Gung, Y., M. Panning, and B. Romanowicz (2003), Global anisotropy and the thickness of continents, *Nature*, *442*, 707–711.

Gutscher, M. A., J. Malavieille, S. Lallemand, and J. Y. Collot (1999a), Tectonic segmentation of the North Andean margin: Impact of the Carnegie Ridge collision, *Earth Planet. Sci. Lett.*, *168*, 255–270.

Gutscher, M. A., J. L. Olivet, D. Aslanian, J. P. Eissen, and R. Maury (1999b), The "lost Inca Plateau": Cause of flat subduction beneath Peru?, *Earth Planet. Sci. Lett.*, *171*, 335–341.

Gutscher, M. A., W. Spakman, H. Bijwaard, and E. R. Engdahl (2000), Geodynamics of flat subduction: Seismicity and tomographic constraints from the Andean margin, *Tectonics*, *19*(5), 814–833.

Hampel, A. (2002), The migration history of the Nazca Ridge along the Peruvian active margin: A re-evaluation, *Earth Planet. Sci. Lett.*, *203*, 665–679.

Hanna, J., and M. D. Long (2012), *SKS* splitting beneath Alaska: Regional variability and implications for subduction processes at a slab edge, *Tectonophysics*, *530–531*, 272–285.

Hayes, G. P., D. J. Wald, and R. L. Johnson (2012), Slab1.0: A three-dimensional model of global subduction zone geometries, *J. Geophys. Res.*, *117*, B01302, doi:10.1029/2011JB008524.

Healy, D., S. M. Reddy, N. E. Timms, E. M. Gray, and A. V. Brovarone (2009), Trench-parallel fast axes of seismic anisotropy due to fluid-filled cracks in subducting slabs, *Earth Planet. Sci. Lett.*, *283*, 75–86.

Heidbach, O., M. Tingay, A. Barth, J. Reinecker, D. Kurfeß, and B. Müller (2008), The World Stress Map database release 2008, doi:10.1594/GFZ.WSM.Rel2008.

Helffrich, G., P. Silver, and H. Given (1994), Shear-wave splitting variation over short spatial scales on continents, *Geophys. J. Int.*, *119*, 561–573.

Henry, S. G., and H. N. Pollack (1988), Terrestrial heat flow above the Andean subduction zone in Bolivia and Peru, *J. Geophys. Res.*, *93*(B12), 15,153–15,162.

Hess, H. H. (1964), Seismic anisotropy of the uppermost mantle under oceans, *Nature*, *203*, 629–631.

Hicks, S. P., S. E. J. Nippress, and A. Rietbrock (2012), Sub-slab mantle anisotropy beneath south-central Chile, *Earth Planet. Sci. Lett.*, *357*, 203–213.

Jung, H., and S. Karato (2001), Water-induced fabric transitions in olivine, *Science*, *293*, 1460–1463.

Kaneshima, S., and P. G. Silver (1995), Anisotropic loci in the mantle beneath central Peru, *Phys. Earth Planet. Inter.*, *88*, 257–272.

Karato, S.-I. (2008), *Deformation of Earth Materials: An Introduction to the Rheology of Solid Earth*, Cambridge Univ. Press, Cambridge, U. K.

Karato, S., H. Jung, I. Katayama, and P. Skemer (2008), Geodynamic significance of seismic anisotropy of the upper mantle: New insights from laboratory studies, *Annu. Rev. Earth Planet. Sci.*, *36*, 59–95.

Katayama, I., H. Jung, and S. Karato (2004), New type of olivine fabric at modest water content and low stress, *Geology*, *32*, 1045–48.

Kirby, S., E. R. Engdahl, and R. Denlinger (1996), Intermediate-depth intraslab earthquakes and arc volcanism as physical expressions of crustal and uppermost mantle metamorphism in subducting slabs, in *Subduction: Top to Bottom*, *Geophys. Monogr. Ser.*, vol. 96, edited by G. E. Bebout, D. Scholl, and S. Kirby, pp. 195–214, AGU, Washington, D. C., doi:10.1029/GM096p0195.

Kneller, E. A., and P. E. van Keken (2007), Trench-parallel flow and seismic anisotropy in the Marianas and Andean subduction systems, *Nature*, *450*, 1222–1225, doi:10.1038/nature06429.

Kneller, E. A., and P. E. van Keken (2008), Effect of three-dimensional slab geometry on deformation in the mantle wedge: Implications for shear wave anisotropy, *Geochem. Geophys. Geosyst.*, *9*, Q01003, doi:10.1029/2007GC001677.

Kneller, E. A., P. E. van Keken, S. Karato, and J. Park (2005), B-type olivine fabric in the mantle wedge: Insights from high-resolution non-Newtonian subduction zone models, *Earth Planet. Sci. Lett.*, *237*, 781–97.

Levin, V., D. Droznin, J. Park, and E. Gordeev (2004), Detailed mapping of seismic anisotropy with local shear waves in southeastern Kamchatka, *Geophys. J. Int.*, *158*(3), 1009–1023, doi:10.1111/j.1365-246X.2004.02352.x.

Long, M. D. (2010), Frequency-dependent shear wave splitting and heterogeneous structure beneath the Gulf of California region, *Phys. Earth Planet. Inter.*, *182*, 59–72.

Long, M. D., and P. G. Silver (2008), The subduction zone flow field from seismic anisotropy: A global view, *Science*, *319*, 315–318.

Long, M. D., and P. G. Silver (2009a), Mantle flow in subduction systems: The sub-slab flow field and implications for mantle dynamics, *J. Geophys. Res.*, *114*, B10312, doi:10.1029/2008JB006200.

Long, M. D., and P. G. Silver (2009b), Shear wave splitting and mantle anisotropy: Measurements, interpretations, and new directions, *Surv. Geophys.*, *30*, 407–461.

Long, M. D., M. H. Benoit, M. C. Chapman, and S. D. King (2010), Upper mantle anisotropy and transition zone thickness beneath southeastern North America and implications for mantle dynamics, *Geochem., Geophys., Geosyst.*, *11*, Q10012, doi:10.1029/2010GC003247.

Long, M. D., L. S. Wagner, S. L. Beck, H. Tavera, B. Bishop, C. M. Eakin, S. Knezevic Antonijevic, A. Kumar, and C. Condori Quispe (2012), Structure and dynamics of the Peruvian flat slab: Results from PULSE, Abstract DI23A-2372 presented at 2012 Fall Meeting, AGU, San Francisco, California, 3–7 Dec.

Lynner, C., and M. D. Long (2012), Evaluating contributions to SKKS splitting from lower mantle anisotropy: A case study from station DBIC, Côte D'Ivoire, *Bull. Seism. Soc. Am.*, *102*, 1030–1040.

Lynner, C., and M. D. Long (2013), Sub-slab seismic anisotropy and mantle flow beneath the Caribbean and Scotia subduction zones: Effects of slab morphology and kinematics, *Earth Planet. Sci. Lett.*, *361*, 367–378.

Maggi, A., E. Debayle, K. Priestley, and G. Barruol (2006), Azimuthal anisotropy of the Pacific region, *Earth Planet. Sci. Lett.*, *250*, 53–71.

Mainprice, D. (2007), Seismic anisotropy of the deep Earth from a mineral and rock physics perspectives, *Treatise on Geophysics*, *2*, 437–491.

Marson-Pidgeon, K., and M. K. Savage (1997), Frequency dependent anisotropy in Wellington, New Zealand, *Geophys. Res. Lett.*, *24*, 3297–3300.

Marson-Pidgeon, K., and M. K. Savage (2004), Modelling shear wave splitting observations from Wellington, New Zealand, *Geophys. J. Int.*, *157*, 853–864.

Martinod, J., L. Husson, P. Roperch, B. Guillaume, and N. Espurt (2010), Horizontal subduction zones, convergence velocity and the building of the Andes, *Earth Planet. Sci. Lett.*, *299*, 299–309.

Meade, C., P. G. Silver, and S. Kaneshima (1995), Laboratory and seismological observations of lower mantle isotropy, *Geophys. Res. Lett.*, *22*(10), 1293–1296, doi:10.1029/95GL01091.

Montagner, J.-P., and T. Tanimoto (1990), Global anisotropy in the upper mantle inferred from regionalization of phase velocities, *J. Geophys. Res.*, *95*(B4), 4797–4819.

Montagner, J.-P., and T. Tanimoto (1991), Global upper mantle tomography of seismic wave velocities and anisotropies, *J. Geophys. Res.*, *96*(B12), 20,337–20,351.

Müller, R. D., M. Sdrolias, C. Gaina, and W. R. Roest (2008), Age, spreading rates and spreading asymmetry of the world's ocean crust, *Geochem. Geophys. Geosys.*, *9*, Q04006, doi:10.1029/2007GC001743.

Nettles, M., and A. M. Dziewonski (2008), Radially anisotropic shear velocity structure of the upper mantle globally and beneath North America, *J. Geophys. Res.*, *113*, B02303, doi:10.1029/2006JB004819.

Nikulin, A., V. Levin, and J. Park (2009), Receiver function study of the Cascadia megathrust: Evidence for localized serpentinization. *Geochem. Geophys. Geosyst.*, *10*, Q07004, doi:10.1029/2009GC002376.

Paczkowski, K. (2012), Dynamic analysis of modifications to simple plate tectonics theory. PhD Thesis, Yale University, 185 pp.

Polet, J., P. G. Silver, S. Beck, T. Wallace, G. Zandt, S. Rupper, R. Kind, and A. Rudloff (2000), Shear wave anisotropy beneath the Andes from the BANJO, SEDA, and PISCO experiments, *J. Geophys. Res.*, *105*(B3), 6287–6304.

Ramos, V. A., and A. Folguera (2009), Andean flat-slab subduction through time, *Geol. Soc. London Spec. Publ.*, *327*(1), 31–54, doi:10.1144/SP327.3.

Rosenbaum, G., D. Giles, M. Saxon, P. G. Betts, R. F. Weinberg, and C. Duboz (2005), Subduction of the Nazca Ridge and the Inca Plateau: Insights into the formation of ore deposits in Peru, *Earth Planet. Sci. Lett.*, *239*, 18–32.

Rümpker, G., and T. Ryberg (2000), "Fresnel-zone" estimates for shear-wave splitting observations from finite-difference modeling, *Geophys. Res. Lett.*, *27*(13), 2005–2008.

Rümpker, G., and P. G. Silver (1998), Apparent shear-wave splitting parameters in the presence of vertically varying anisotropy, *Geophys. J. Int.*, *135*, 790–800.

Russo, R. M. (2009), Subducted oceanic asthenosphere and upper mantle flow beneath the Juan de Fuca slab, *Lithosphere*, *1*, 195–205.

Russo, R. M., and P. G. Silver (1994), Trench-parallel flow beneath the Nazca Plate from seismic anisotropy, *Science*, *263*, 1105–1111.

Saltzer, R. L., J. Gaherty, and T. H. Jordan (2000), How are vertical shear wave splitting measurements affected by variations in the orientation of azimuthal anisotropy with depth?, *Geophys. J. Int.*, *141*, 374–390.

Savage, M. K. (1999), Seismic anisotropy and mantle deformation: What have we learned from shear wave splitting, *Rev. Geophys.*, *37*(1), 65–106.

Siebert, L., and T. Simkin (2002), *Volcanoes of the World: An Illustrated Catalog of Holocene Volcanoes and Their Eruptions*. *Global Volcanism Program Digital Information Series*, *GVP-3*, Smithsonian Institution, Washington, D. C., (Available at http://www.volcano.si.edu/world/).

Silver, P. G., and W. W. Chan (1991), Shear wave splitting and subcontinental mantle deformation, *J. Geophys. Res.*, *96*, 16,429–16,454.

Silver, P. G., and M. K. Savage (1994), The interpretation of shear-wave splitting parameters in the presence of two anisotropic layers, *Geophys. J. Int.*, *119*, 949–963.

Skinner, S., and R. W. Clayton (2011), An evaluation of proposed mechanisms of slab flattening in Central Mexico, *Pure Appl. Geophys.*, *168*, 1461–1474.

Skinner, S., and R. W. Clayton (2013), The lack of correlation between flat slabs and bathymetric impactors in South America, *Earth Planet. Sci. Lett.*, *371*, 1–5.

Song, T.-R. A., and H. Kawakatsu (2012), Subduction of oceanic asthenosphere: Evidence from sub-slab seismic anisotropy, *Geophys. Res. Lett.*, *39*, L17301, doi:10.1029/2012GL052639.

Song, T.-R. A., and H. Kawakatsu (2013), Subduction of oceanic asthenosphere: A critical appraisal in central Alaska, *Earth Planet. Sci. Lett.*, *367*, 82–94.

Song, T.-R. A., and Y. Kim (2012), Anisotropic upper mantle in young subducted slab underplating Central Mexico, *Nat. Geosci.*, *5*, 55–59.

Tono, Y., and Y. Fukao (2013), Shear-wave splitting apparently caused by contamination of *P*-to-*S* or *S*-to-*P* converted waves, *Bull. Seism. Soc. Am.*, *103*, 950–957.

van Hunen, J., A. van den Berg, and N. J. Vlaar (2002), On the role of subducting oceanic plateaus in the development of shallow flat subduction, *Tectonophysics*, *352*, 317–333.

Vidale, J. E. (1986), Complex polarization analysis of particle motion, *Bull. Seism. Soc. Am.*, *71*, 1511–1530.

Walker, A. M., and J. Wookey (2012), MSAT—A new toolkit for the analysis of elastic and seismic anisotropy, *Computers & Geosciences*, *49*, 81–90.

Wirth, E., and M. D. Long (2010), Frequency-dependent shear wave splitting beneath the Japan and Izu-Bonin subduction zones, *Phys. Earth Planet. Inter.*, *181*, 141–154.

Wirth, E., and M. D. Long (2012), Multiple layers of seismic anisotropy and a low-velocity region in the mantle wedge beneath Japan: Evidence from teleseismic receiver functions, *Geochem. Geophys. Geosyst.*, *13*, Q08005, doi:10.1029/2012GC004180.

Wüstefeld, A., and G. Bokelmann (2007), Null detection in shear-wave splitting measurements, *Bull. Seism. Soc. Am.*, *97*, 1204–1211.

Wüstefeld, A., G. Bokelmann, C. Zaroli, and G. Barruol (2008), SplitLab: A shear-wave splitting environment in Matlab, *Computers & Geosciences*, *34*, 515–528.

Zhang, S., and S. I. Karato (1995), Lattice preferred orientation of olivine aggregates deformed in simple shear, *Nature*, *375*, 774–777.